

Connection between Macroscopic Hydrodynamics and Molecular Friction in Liquids

Henrik Kiefer,^{*} Benjamin A. Dalton,[†] Florian N. Brünig,[‡] and Roland R. Netz[§]
Freie Universität Berlin, Department of Physics, Arnimallee 14, 14195 Berlin, Germany.

(Dated: January 13, 2022)

A fundamental problem in molecular dynamics is the relation between the frequency-dependent friction of a molecule in a liquid and the underlying hydrodynamic equations. We investigate this connection for the case of a water molecule moving in liquid water using all-atomistic molecular dynamics simulations and linear hydrodynamic theory. For this we calculate the frequency-dependent friction of a sphere with finite surface slip moving in a non-Newtonian compressible fluid by solving the linear transient Stokes equation, including frequency-dependent shear and volume viscosities, which are determined from MD simulations of bulk liquid water. We investigate in detail the influence of the volume viscosity on the sphere friction and find that the high-frequency decay of the volume viscosity crucially influences the friction. We also determine the frequency-dependent friction of a single water molecule moving in liquid water, as defined by the generalized Langevin equation, from MD simulation trajectories. By fitting the effective sphere radius and the slip length in the solution of the Stokes equation, the two frequency-dependent frictions are shown to agree well. This shows that the transient Stokes equation describes the frequency-dependent friction of a single water molecule in liquid water and thus applies down to molecular length and time scales, provided accurate frequency-dependent viscosities are used. In particular the pronounced maximum of the sphere friction around 7 THz is shown to be caused by a pronounced maximum of the shear viscosity at the same frequency. We also find non-negligible slip effects for the motion of a water molecule, in quantitative agreement with a recent study of the translational and rotational diffusion of a water molecule in liquid water. For a methane molecule moving in water, the friction function cannot be predicted based on our simple hydrodynamic model, which suggests that a methane molecule is surrounded by a hydration layer with viscous properties that are very different from bulk water.

Subject Areas: Soft Matter, Statistical Physics, Fluid Dynamics, Biological Physics, Complex Systems

I. INTRODUCTION

The friction force acting on a solute molecule in a liquid environment exhibits a delayed non-Markovian response due to the finite relaxation time of the solvating liquid degrees of freedom [1–4]. Such memory effects occur on time scales that range between sub-picoseconds up to microseconds and even seconds, depending on the type and complexity of the system [5–9]. Including time- or frequency-dependent friction in an appropriate theoretical framework allows for the accurate modeling of macromolecular dynamics in liquid environments [10, 11] and for the proper viscoelastic description of soft matter [12–14]. An important issue is the connection between the macroscopic hydrodynamic equations and the microscopic friction acting on a particle or a molecule in a fluid. Numerous studies investigated this connection by comparing the friction acting on a particle, as described by the generalized Langevin equation, with the friction obtained by solving the fluid flow around a spherical particle using hydrodynamic equations [15–24]. Pioneering work in this direction was done by Zwanzig et al. [25] and later by Metiu et al. [26], who obtained the time- or frequency-dependent friction by solving the

linearized Stokes equation for a spherical particle in the presence of a frequency-dependent shear viscosity, which was described by a Maxwell model with a single relaxation time. Since a considerable discrepancy between the friction obtained from the solution of the Stokes equation and the friction derived from the velocity autocorrelations obtained in molecular dynamics simulations was found, especially at high frequencies, it was concluded that hydrodynamic theory does not work on molecular time and length scales. In fact, a critical limitation in that comparison is that a Maxwell model with a single relaxation time was used for the shear viscosity in the solution of the Stokes equation. However, viscosity spectra measured in experiments [27, 28] and extracted from molecular dynamics (MD) simulations of water [29–31], indicate pronounced deviations from a simple Maxwell model, especially at high frequencies in the THz regime. This is the frequency range where deviations between the friction from hydrodynamic predictions and from molecular simulation were found, so that it is not clear whether hydrodynamic theory breaks down or whether an inappropriate model for the shear viscosity was used.

In the present work, we reconsider the connection between macroscopic hydrodynamics and the microscopic friction acting on a single water molecule in a liquid water environment. For this, we first derive the frequency-dependent friction acting on a sphere using the linearized Stokes equation using frequency-dependent shear and volume viscosities, finite compressibility and a finite surface slip [32]. In contrast to previous work [22, 24, 26], we do not use a phenomenological Maxwell model for

^{*} henrik.kiefer@fu-berlin.de

[†] daltonr@fu-berlin.de

[‡] florian.brueinig@fu-berlin.de

[§] rnetz@fu-berlin.de

the shear viscosity but rather use frequency-dependent shear and volume viscosities extracted from MD simulations. We in detail investigate the influence of the frequency-dependence of the volume viscosity on the friction function at high frequencies. We compare the friction from the Stokes equation with the friction extracted from MD simulations of a freely moving water molecule in liquid water using the framework of the generalized Langevin equation. Using the surface slip parameter and the sphere radius that appear in the hydrodynamic prediction of the friction as free fit parameters, we find that the friction of a water molecule extracted directly from MD simulations is in good agreement with the hydrodynamic predictions. This establishes the long-sought link between macroscopic hydrodynamics and the friction of a molecule in a fluid. It turns out the macroscopic shear viscosity shows pronounced multi-mode behavior as a function of frequency and thus cannot be described by a Maxwell model with a single relaxation time, which explains why previous attempts to derive molecular friction from hydrodynamic theory failed. The fitted radius and slip length obtained from our comparison agree with recent results from MD simulations of the translational and rotational diffusivities of a water molecule in liquid water, which demonstrates that our approach is physically sound. We thus find that the macroscopic hydrodynamic equations work surprisingly well down to molecular time and spatial scales for homogeneous liquids, i.e. if one considers the motion of a single water molecule embedded in liquid water. However, we also observe that the friction of methane in liquid water cannot be described by hydrodynamic theory using liquid water shear and volume viscosities. This indicates that for inhomogeneous liquids, i.e. for the motion of a molecule that differs from the surrounding liquid, the simple hydrodynamic model has to be generalized in order to account for the modified viscosity of the solvation layer around a moving host molecule.

II. THEORY

A. Friction of a Sphere from Hydrodynamic Theory

A general expression for the friction of a sphere in a liquid is derived by using the fundamental equations of hydrodynamics [33–35]. The Navier-Stokes equation, i.e. the equation for local momentum conservation reads

$$\frac{\partial \rho(\vec{r}, t) v_i(\vec{r}, t)}{\partial t} + \nabla_j \rho(\vec{r}, t) v_i(\vec{r}, t) v_j(\vec{r}, t) = F_i(\vec{r}, t) + \nabla_j \sigma_{ij}(\vec{r}, t), \quad (1)$$

where $i, j \in \{x, y, z\}$. The density ρ , the velocity v_i , and the volume force F_i are functions of time t and position \vec{r} . The symmetric stress tensor $\sigma_{ij}(\vec{r}, t)$ consists of diagonal pressure contributions and components that depend on

velocity gradients, i.e. $\nabla_j v_i(\vec{r}, t)$ [31, 36–38]. For a linear, homogeneous, isotropic compressible fluid it is given by

$$\begin{aligned} \sigma_{ij}(\vec{r}, t) = & -P(\vec{r}, t) \delta_{ij} \\ & + \int \int \left[\eta(|\vec{r}'|, t') \left(\nabla_i v_j(\vec{r} - \vec{r}', t - t') \right. \right. \\ & \left. \left. + \nabla_j v_i(\vec{r} - \vec{r}', t - t') \right) \right. \\ & \left. + \delta_{ij} \left(\zeta(|\vec{r}'|, t') - \frac{2}{3} \eta(|\vec{r}'|, t') \right) \nabla_k v_k(\vec{r} - \vec{r}', t - t') \right] d\vec{r}' dt', \end{aligned} \quad (2)$$

where $P(\vec{r}, t)$ is the pressure, and η and ζ are the shear and volume viscosity kernels, which we assume to be time- and space-dependent. If the viscosity kernels decay on length- and time scales that are small compared to those on which $\nabla_j v_i(\vec{r}, t)$ varies, one can approximate the stress tensor in Eq. 2 as

$$\begin{aligned} \sigma_{ij}(\vec{r}, t) \approx & -P(\vec{r}, t) \delta_{ij} + \zeta_0 \delta_{ij} \nabla_k v_k(\vec{r}, t) \\ & + \eta_0 \left(\nabla_i v_j(\vec{r}, t) + \nabla_j v_i(\vec{r}, t) - \frac{2}{3} \delta_{ij} \nabla_k v_k(\vec{r}, t) \right), \end{aligned} \quad (3)$$

where η_0 and ζ_0 are the time- and space-independent viscosities

$$\eta_0 = \int \int \eta(|\vec{r}'|, t') d\vec{r}' dt', \quad (4)$$

$$\zeta_0 = \int \int \zeta(|\vec{r}'|, t') d\vec{r}' dt'. \quad (5)$$

We define a fluid with a stress tensor given by Eq. 3 as a Newtonian fluid, and we will explicitly consider non-Newtonian fluids in this work.

If we neglect the non-linear term (second term on the left-hand side in Eq. 1) in the Navier-Stokes equation, which is justified for low Reynolds numbers, and use the the expression of the stress tensor in Eq. 2, we arrive at the linear transient Stokes equation

$$\begin{aligned} \rho(\vec{r}, t) \frac{\partial v_i(\vec{r}, t)}{\partial t} = & F_i(\vec{r}, t) - \nabla_i P(\vec{r}, t) \\ & + \int \int \left(\frac{1}{3} \eta(|\vec{r}'|, t') + \zeta(|\vec{r}'|, t') \right) \nabla_i \nabla_k v_k(\vec{r} - \vec{r}', t - t') d\vec{r}' dt' \\ & + \int \int \eta(|\vec{r}'|, t') \nabla_k \nabla_k v_i(\vec{r} - \vec{r}', t - t') d\vec{r}' dt'. \end{aligned} \quad (6)$$

The volume viscosity $\zeta(t)$ quantifies a fluid's response to compression [39] and is crucial for describing processes such as sound propagation or shock waves [30], and can be calculated from the autocorrelation of instantaneous pressure fluctuations. On the other hand, the shear viscosity $\eta(t)$ is calculated from the autocorrelation of the trace-less stress tensor. Often, the volume viscosity is neglected, which corresponds to the Stokes hypothesis, which states that the volume viscosity is defined as $\zeta = \lambda' + 2\eta/3$, where λ' is the so-called Lamé factor [40, 41]. Specifically, Stokes postulated $\lambda' = -2\eta/3$ and hence $\zeta = 0$. However, in previous simulations and experiments, it was found that the volume viscosity for water is non-negligible and can even be greater than

the shear viscosity [42]. Thus, we explicitly consider a non-vanishing volume viscosity. The Stokes equation in Eq. 6 can be analytically solved by calculating its Green's function. From the Green's function, we can construct the frequency-dependent friction of a sphere, $\tilde{\Gamma}^{hyd}(\omega)$, a complex-valued function encoding the macroscopic fluid's stress response to a small, oscillatory sphere motion

$$\delta_{ij}\tilde{\Gamma}^{hyd}(\omega) = \frac{\tilde{F}_i^{sp}(\omega)}{\tilde{V}_j^{sp}(\omega)}, \quad (7)$$

where $\tilde{V}_j^{sp}(\omega)$ is the frequency-dependent velocity of the sphere and $\tilde{F}_i^{sp}(\omega)$ is the hydrodynamic force acting on the sphere. We define the spatial and temporal Fourier transformation (FT) of a function f as $f(\vec{r}, t) = (2\pi)^{-4} \int d\omega d^3k \tilde{f}(\vec{k}, \omega) e^{i(k_i r_i + \omega t)}$. The friction function of a spherical particle is given by

$$\tilde{\Gamma}^{hyd}(\omega) = \frac{4\pi\tilde{\eta}(\omega)aW}{3} \left\{ (1 + \hat{\lambda})(9 + 9\hat{\alpha} + \hat{\alpha}^2)(1 + 2\hat{b}) + (1 + \hat{\alpha})[2\hat{\lambda}^2(1 + 2\hat{b}) + \hat{b}\hat{\alpha}^2(1 + \hat{\lambda})] \right\}. \quad (8)$$

where a is the spherical radius and W is given by

$$W = (2 + 2\hat{\lambda} + \hat{\lambda}^2)(1 + \hat{b}(3 + \hat{\alpha})) + (1 + \hat{\alpha})(1 + 2\hat{b})\hat{\lambda}^2/\hat{\alpha}^2. \quad (9)$$

In Appendix A, we show the derivation of Eq. 8, in the presence of a finite slip at the spherical surface, described by the dimensionless slip length, $\hat{b} = b/a$. The dimensionless decay constants $\hat{\alpha} = a\alpha$ and $\hat{\lambda} = a\lambda$ are defined by

$$\alpha^2(\omega) = i\omega\rho_0/\tilde{\eta}(\omega), \quad (10)$$

and

$$\lambda^2(\omega) = \frac{i\omega\rho_0}{4\tilde{\eta}(\omega)/3 + \tilde{\zeta}(\omega) - i\rho_0c^2/\omega}, \quad (11)$$

where c is the speed of sound. From Eq. 8-11, we see that there is a direct relationship between the friction $\tilde{\Gamma}^{hyd}(\omega)$ and the shear and volume viscosities $\tilde{\eta}(\omega)$ and $\tilde{\zeta}(\omega)$. The low- and high-frequency behavior of $\tilde{\Gamma}^{hyd}$ is therefore fundamentally determined by the frequency-dependence of both viscosities. In Appendix B, we discuss the behavior of the sphere friction for frequency-independent viscosities. In the main part of this work, however, we deal with frequency-dependent viscosities.

B. Particle Friction From the Generalized Langevin Equation

For a particle with mass m , the dynamics can be described by the generalized Langevin equation (GLE) [1, 2, 8]

$$m\ddot{\vec{x}}(t) = -\vec{\nabla}U[\vec{x}(t)] - \int_0^\infty dt' \Gamma(t-t')\dot{\vec{x}}(t') + \vec{F}_R(t), \quad (12)$$

where $-\nabla U[\vec{x}(t)]$ is the force due to a potential, $\Gamma(t)$ the friction function, often called the memory kernel, and $\vec{F}_R(t)$ the random force, which can be assumed to follow a stationary Gaussian process with zero mean and variance

$$\langle \vec{F}_R(t)\vec{F}_R^T(t') \rangle = k_B T \Gamma(|t-t'|)I, \quad (13)$$

where I is the identity matrix, $k_B T$ the thermal energy with the Boltzmann constant k_B and the absolute temperature T . The static friction between the particle with its environment γ_0 is determined by the integral of the memory kernel, i.e. $\gamma_0 = \int_0^\infty \Gamma(t)dt$.

We assume isotropic fluids and thus consider only one component of the particle motion i.e. $\vec{x}(t) \equiv x(t)$. In Fourier space and for $\nabla U = 0$, the GLE in Eq. 12 reads

$$\tilde{v}(\omega) = \frac{\tilde{F}_R(\omega)}{\tilde{\Gamma}_+(\omega) + i\omega m}, \quad (14)$$

where we use the single-sided memory function $\Gamma_+(t) = \Gamma(t)$ for $t \geq 0$, and $\Gamma_+(t) = 0$ for $t < 0$. In Appendix C, we show by calculating the fluid momentum outside a moving sphere from the transient Stokes equation in Eq. 6 that the hydrodynamic friction $\tilde{\Gamma}^{hyd}(\omega)$ in Eq. 8 does not include inertial effects inside the sphere. Thus, by comparing Eqs. 7 and Eq. 14 we can conclude that $\tilde{\Gamma}^{hyd}(\omega)$ and $\tilde{\Gamma}_+(\omega)$ describe the friction response of the fluid surrounding the sphere and therefore can be directly compared to each other.

III. RESULTS AND DISCUSSION

A. Friction of a Single Water Molecule from MD Simulations

We analyze MD simulations for the SPC/E and TIP4P/2005 water models (see Appendix D for simulation details). Specifically, we extract memory kernels from the motion of a water molecule in pure liquid water, for the force-free case, i.e. $\nabla U = 0$, in Eq. 12 (see Appendix E for the procedure).

In fig. 1 (A), we show the extracted memory kernel $\Gamma(t)$ of a water molecule in water for both water models, which differ only marginally and show exponential decays and oscillations, indicative of dissipative effects at different time scales [43]. In fig. 1 (B,C), we show the computed real and imaginary single-sided Fourier transformation of the memory kernels $\tilde{\Gamma}_+(\omega)$, obtained by fast Fourier transformation (FFT). We fit the memory kernels by a sum of five exponential-oscillatory functions

$$\Gamma_+(t) = \Theta(t) \left\{ \sum_{j=1}^V \frac{\gamma_{0,j}\tau_{n,j}}{\tau_{o,j}^2} e^{-t/2\tau_{n,j}} \left[\frac{1}{\kappa_j} \sin\left(\frac{\kappa_j}{2\tau_{n,j}}t\right) + \cos\left(\frac{\kappa_j}{2\tau_{n,j}}t\right) \right] \right\}, \quad (15)$$

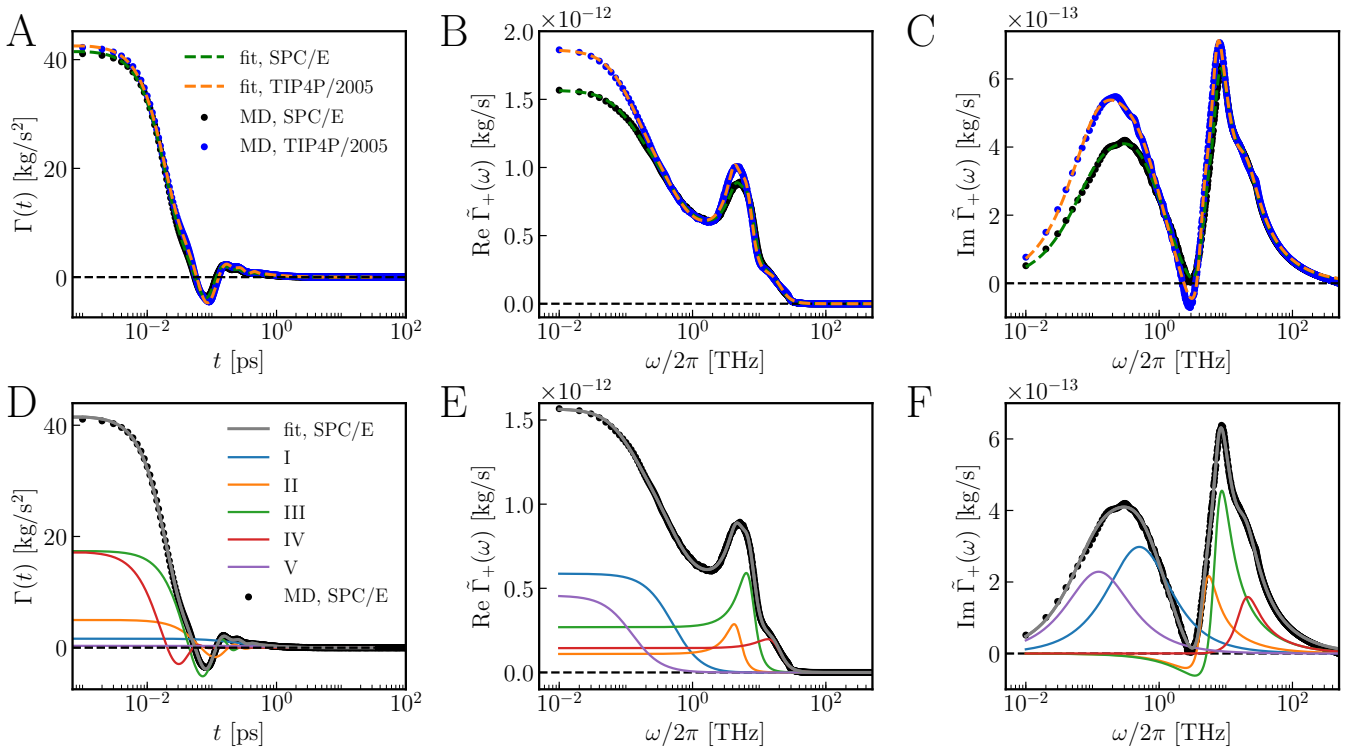


FIG. 1. Extracted memory kernels $\Gamma(t)$ of a single water molecule in water from MD simulations of SPC/E and TIP4P/2005 water. A: Memory kernel in the time domain with fits according to Eq. 15 and the fitting parameters in tab. I (Appendix H). B, C: Real and imaginary parts of the memory kernel in the frequency domain with fits according to Eq. 16. D - F: Individual fitting components according to Eqs. 15 and 16 for the SPC/E water model.

or in frequency domain

$$\tilde{\Gamma}_+(\omega) = \sum_{j=I}^V \gamma_{0,j} \frac{1 - i\omega\tau_{n,j}}{1 - i\omega\tau_{o,j}^2/\tau_{n,j} - \omega^2\tau_{o,j}^2}, \quad (16)$$

where $\kappa_j = \sqrt{4(\tau_{n,j}/\tau_{o,j})^2 - 1}$. These memory functions can be derived from the Hamilton equations of motion [44, 45], for a reaction coordinate $x(t)$ with mass m that is linearly coupled to an auxiliary coordinate $y(t)$ with mass m_y (see Appendix F). Depending on κ , the memory kernel displays a single-exponential decay with oscillations (finite real part of κ), or is a sum of two exponential decays (imaginary κ). A single-exponential memory kernel, i.e. $\Gamma_+(t) = \Theta(t)(\gamma_0/\tau)e^{-t/\tau}$ with decay constant τ follows from the exponential-oscillatory memory kernel in Eq. 15 in the mass-less limit, i.e. $m_y \rightarrow 0$ (see Appendix G). In fig. 1 (A, B, C), we show the best fit for the MD data of the two water models (dashed lines). The fitting values are given in tab. I in Appendix H, the fitting algorithm is described in Appendix I. We observe good agreement between the data and the fitting model over several orders in the time and the frequency domain. The components I and V are overdamped (imaginary κ), where component V covers the long-time decay of the memory kernel (see fig. 1 (D, E, F)). In addition, we observe three underdamped, oscillating components II-IV. For high frequencies, the real part of a exponential-

oscillatory memory kernel in Eq. 16 decays as $\sim 1/\omega^4$ and the imaginary part as $\sim 1/\omega$. We discuss discrepancies of the high-frequency behavior between the memory kernel extracted from the MD simulation and the fit function in Eq. 15 in Appendix J and K, where we show that the high-frequency behavior of the data can be described by memory kernels with exponential or Gaussian high-frequency scaling. The calculated steady-state friction coefficients γ_0 obtained from the fits ($\gamma_0 = \sum_{j=I}^V \gamma_{0,j} = 1.57 \cdot 10^{-12}$ kg/s for SPC/E and $1.87 \cdot 10^{-12}$ kg/s for TIP4P/2005) are in good agreement with previous MD simulation results ($1.53 \cdot 10^{-12}$ kg/s at 300 K for SPC/E [8] and $1.87 \cdot 10^{-12}$ kg/s at 300 K for TIP4P/2005 [46]), and are identical to the plateau values of the running integral of the memory kernels (see Appendix L). Our result for the friction coefficient of TIP4P/2005 water is also in good agreement with experimental results at 298.15 K which are between $1.79 \cdot 10^{-12}$ kg/s [47] and $1.85 \cdot 10^{-12}$ kg/s [48].

B. Frequency-Dependent Shear and Volume Viscosities

The Newtonian fluid as defined in Eq. 3 is a standard model to describe large-scale and long-time hydrodynam-

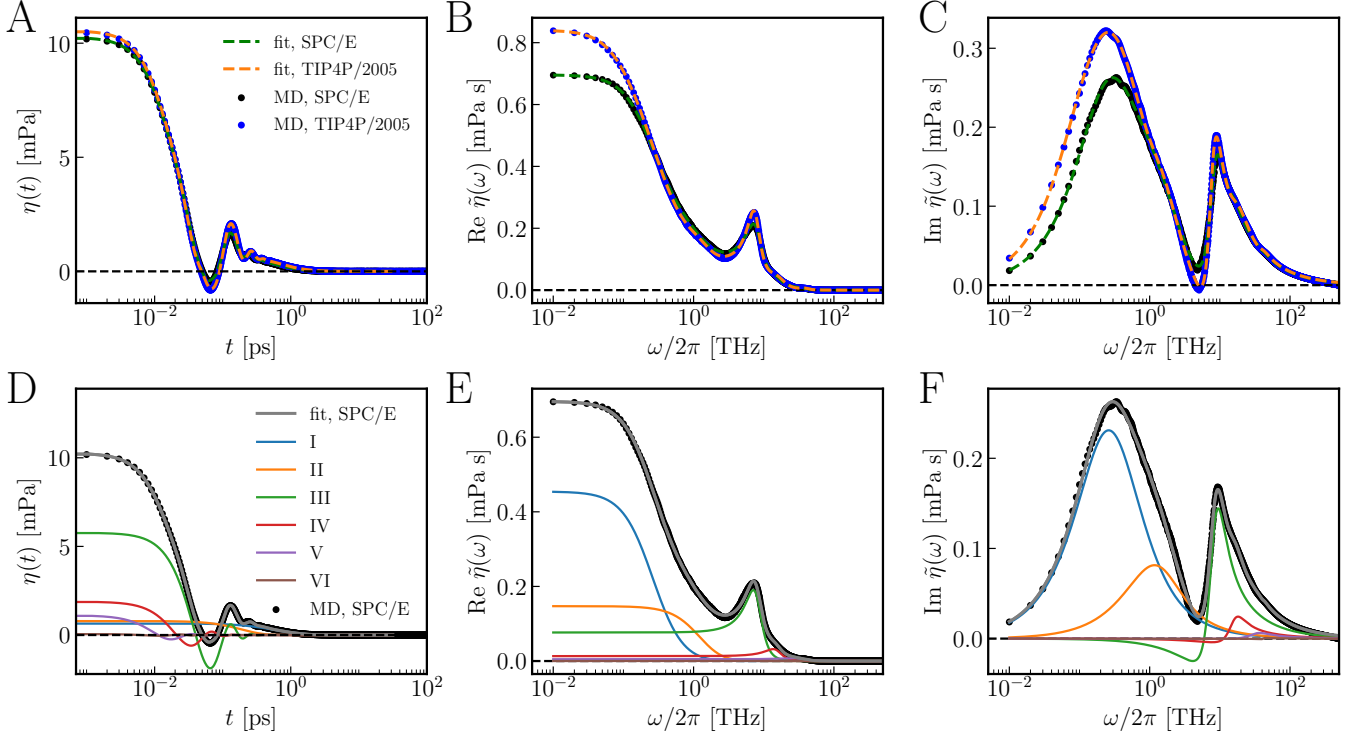


FIG. 2. Extracted shear viscosity $\eta(t)$ from MD simulations of SPC/E and TIP4P/2005 water. A: Shear viscosity in the time domain with fits according to Eq. 17 and fitting parameters in tab. II (Appendix H). B, C: Real and imaginary parts of the shear viscosity in the frequency domain with fits according to Eq. 18. D - F: Individual fitting components according to Eqs. 17, 18 for the SPC/E water model.

ics of liquid water [34, 50, 51]. In earlier experimental investigations and MD simulations, it was found that at high frequencies, typically in the THz regime, liquid water deviates from the Newtonian fluid model [27, 28, 52–60], and that the shear viscosity decreases at high frequencies [31]. In this work, we use calculated shear and volume viscosity spectra extracted from SPC/E and TIP4P/2005 water model simulations (see Appendix M). In fig. 2 (A, B, C), we show the calculated shear viscosity in the time and frequency domain from both water models. Inspired by our findings for the single-water memory kernel in fig. 1, we fit the shear viscosity with a sum of six exponential-oscillating functions

$$\eta(t) = \Theta(t) \left\{ \sum_{j=I}^{VI} \frac{\eta_{0,j} \tau_{n,j}}{\tau_{o,j}^2} e^{-t/2\tau_{n,j}} \left[\frac{1}{\kappa_j} \sin\left(\frac{\kappa_j}{2\tau_{n,j}} t\right) + \cos\left(\frac{\kappa_j}{2\tau_{n,j}} t\right) \right] \right\}, \quad (17)$$

where $\kappa_j = \sqrt{4(\tau_{n,j}/\tau_{o,j})^2 - 1}$, which in the frequency domain reads as

$$\tilde{\eta}(\omega) = \sum_{j=I}^{VI} \eta_{0,j} \frac{1 - i\omega\tau_{n,j}}{1 - i\omega\tau_{o,j}^2/\tau_{n,j} - \omega^2\tau_{o,j}^2}, \quad (18)$$

as described in Appendix I. For both water models, we observe excellent agreement with the MD data in fig. 2

(A, B, C). In tab. II in Appendix H, we provide the fit parameters. Additionally, we show the individual components from the fits of the SPC/E shear viscosity in fig. 2 (D, E, F). As the results show, the TIP4P/2005 model spectra are qualitatively very similar to the SPC/E model, and both exhibit a pronounced peak in the real- and imaginary parts around 7-8 THz. The value of the total steady-state shear viscosity for the SPC/E model of $\eta_0 = \sum_j \eta_{0,j} = 0.70$ mPa s is in close agreement with previous simulations [8], and is lower than the value $\eta_0 = 0.84$ mPa s for the TIP4P/2005 model, in agreement with earlier simulations [30, 61].

Our shear viscosity model includes high-frequency modes V and VI above 20-30 THz, which we identify, by comparison with absorption spectra of simulated water [59] and shear viscosity spectra [31], with librational modes, i.e. rotational vibrations of individual molecules. The oscillation components I and II, which are due to (I) hydrogen-bond network topology changes and (II) hydrogen-bond stretch vibrations of water pairs, are overdamped [31]. A dominant peak emerges from the oscillation time $\tau_{o,III}$ and the memory time $\tau_{n,III}$ from the exponential-oscillatory component III. It results in a resonance frequency of

$$f_{r,III} = \frac{1}{2\pi} \sqrt{\frac{1}{2\tau_{o,III}^2} - \frac{\tau_{n,III}^2}{\tau_{o,III}^4}} \approx 7.11 \text{ THz}, \quad (19)$$

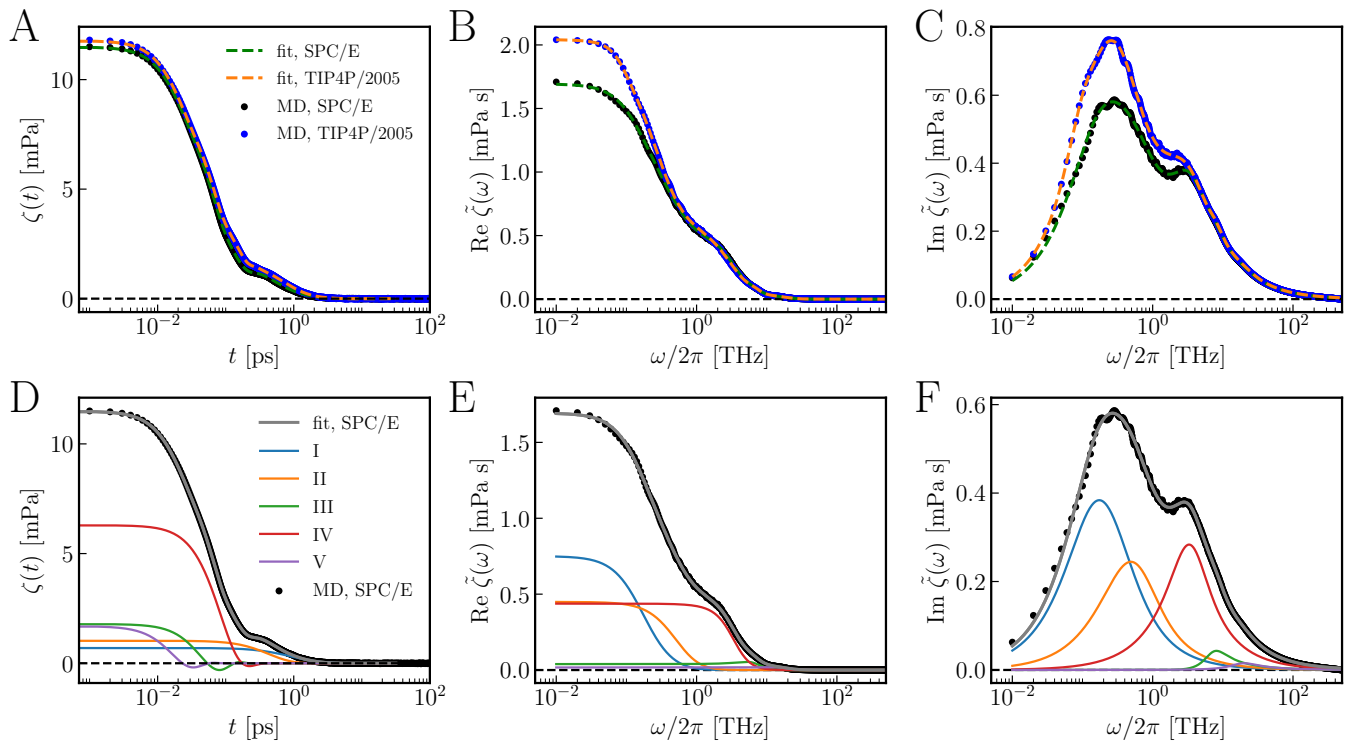


FIG. 3. Extracted volume viscosity $\zeta(t)$ from MD simulations of SPC/E and TIP4P/2005 water. A: Volume viscosity in the time domain with fits according to Eq. 20 and fitting parameters in tab. III (Appendix H). B, C: Real and imaginary parts of the volume viscosity in the frequency domain with fits according to Eq. 21. D - F: Individual fitting components according to Eqs. 20, 21 for the SPC/E water model.

which we obtain from the maximum value of component III in Eq. 18 and is in agreement with frequencies of collective vibrations of hydrogen-bonded water pairs obtained from infrared spectroscopy simulation studies (6.9 THz, from [62]).

In fig. 3, we show the volume viscosity extracted from the MD data, which we determined from the autocorrelation of the pressure fluctuations. The real part of these spectra exhibits no peak in the THz regime, contrary to the shear viscosity, and in agreement with previous simulation results [30]. We fit the volume viscosity data with a sum of five components

$$\zeta(t) = \Theta(t) \left\{ \sum_{j=I}^V \frac{\zeta_{0,j} \tau_{v,j}}{\tau_{w,j}^2} e^{-t/2\tau_{v,j}} \left[\frac{1}{\kappa_j} \sin\left(\frac{\kappa_j}{2\tau_{v,j}} t\right) + \cos\left(\frac{\kappa_j}{2\tau_{v,j}} t\right) \right] \right\}, \quad (20)$$

where $\kappa_j = \sqrt{4(\tau_{v,j}/\tau_{w,j})^2 - 1}$. The total complex volume viscosity in the frequency domain is given by

$$\tilde{\zeta}(\omega) = \sum_{j=I}^V \zeta_{0,j} \frac{1 - i\omega\tau_{v,j}}{1 - i\omega\tau_{w,j}^2/\tau_{v,j} - \omega^2\tau_{w,j}^2}. \quad (21)$$

All components, except for components III and V, are overdamped. We find a steady-state value of $\zeta_0 =$

$\sum_j \zeta_{0,j} = 1.69$ mPa s for the SPC/E and 2.04 mPa s for the TIP4P/2005 model, slightly lower than the experimental value (2.4 mPa s for 298 K [42]) and comparable to results from previous MD simulations [30]: for TIP4P/2005 water simulations $\zeta_0 = 2.07$ mPa s at 298 K and $\zeta_0 = 2.01$ mPa s at 303 K, and for SPC/E water $\zeta_0 = 1.57$ mPa s at 298 K and $\zeta_0 = 1.45$ mPa s at 303 K.

C. Frequency-Dependent Friction of a Spherical Particle from Hydrodynamic Theory

We insert the shear and volume viscosity spectra from the SPC/E water model MD simulations in fig. 2 and fig. 3 into Eq. 8 to compute the friction of a sphere. In fig. 4, we show the friction $\tilde{\Gamma}^{hyd}(\omega)$ for different values of the sphere radius a and slip coefficient $\hat{b} = b/a$. Note that the results are normalized by $6\pi a \eta_0$ with $\eta_0 = \sum_j \eta_{0,j} = 0.70$ mPa s, which is the static friction for zero slip. We compare results for finite frequency-independent volume viscosity $\zeta_0 = \sum_j \zeta_{0,j} = 1.69$ mPa s (dashed lines), for vanishing volume viscosity $\zeta_0 = 0$ (dotted lines) and for frequency-dependent volume viscosity from fig. 3 (solid lines).

For small radii ($a = 10^{-12}$ m and $a = 10^{-10}$ m), the friction $\tilde{\Gamma}^{hyd}(\omega)$ in fig. 4 exhibits similar features as the

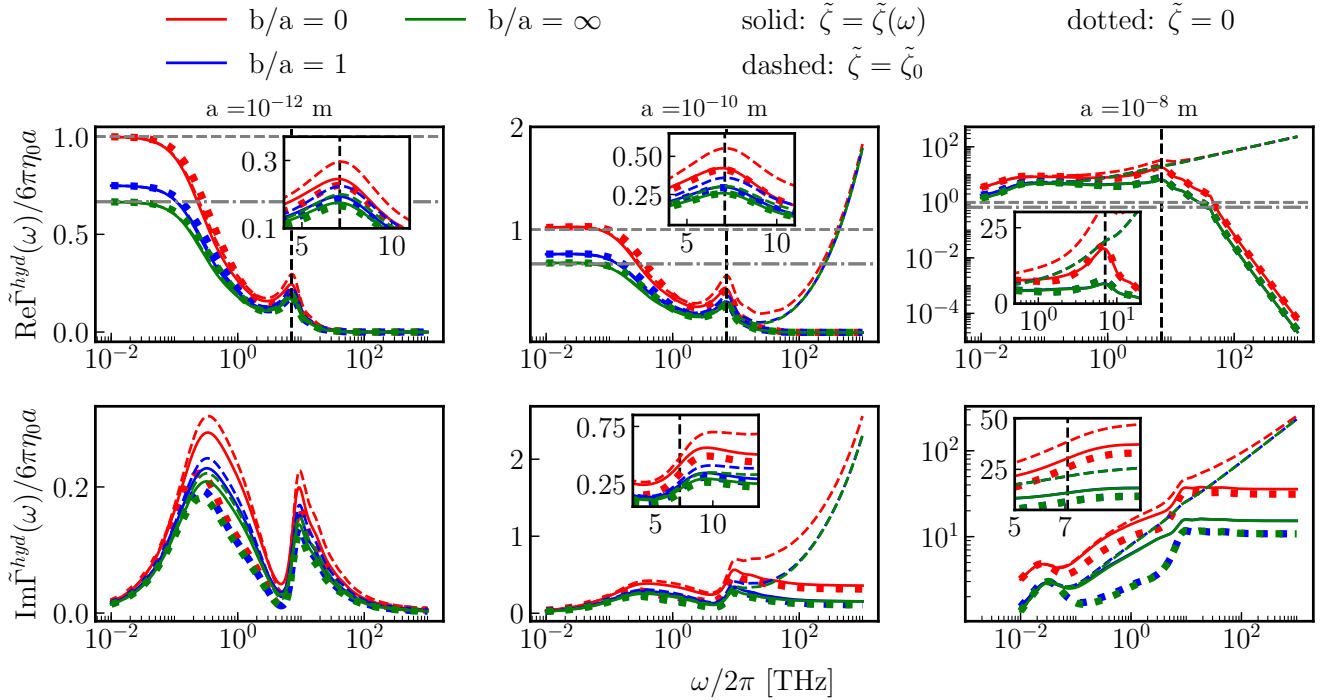


FIG. 4. Real and imaginary parts of the rescaled friction function of a sphere $\tilde{\Gamma}^{hyd}(\omega) = \text{Re } \tilde{\Gamma}^{hyd}(\omega) + i \text{Im } \tilde{\Gamma}^{hyd}(\omega)$, given by Eq. 8 for various normalized slip lengths $\hat{b} = b/a$ and in dependence of the sphere radius a . Here we use the viscoelastic model for the shear viscosity $\tilde{\eta}(\omega)$ in Eq. 18 for pure water in fig. 2. We use the shear viscosity model with fits from the SPC/E water model. The results are normalized by the steady-state viscosity $\eta_0 = \sum_j \eta_{0,j} = 0.70$ mPa s. We set the water density to $\rho = 10^3$ kg/m³ and the speed of sound to $c = 1.51 \cdot 10^3$ m/s [49]. We show the results with frequency-independent volume viscosity $\zeta_0 = \sum_j \zeta_{0,j} = 1.69$ mPa s (dashed lines), with vanishing volume viscosity ($\zeta = 0$, dotted lines) and with the fitted model of the frequency-dependent result in fig. 3 (A) (solid lines). We provide figure insets for a better visibility at frequencies where the data lie close together. The horizontal lines denote the $\omega \rightarrow 0$ limits expected by standard steady-state results [33], to $6\pi\eta_0a$ for $\hat{b} \rightarrow 0$ and to $4\pi\eta_0a$ for $\hat{b} \rightarrow \infty$, respectively. The vertical dashed line denotes the pronounced oscillation with resonance frequency $f_{r,III} \approx 7.11$ THz (Eq. 19) from the viscoelastic exponential-oscillatory model in fig. 2.

frequency-dependent shear viscosity in fig. 2 and in particular shows a peak around 7 THz, denoted as vertical dashed line in fig. 4. For large frequencies, we see that the real part of the friction diverges for constant volume viscosity and goes to zero for frequency-dependent ($\tilde{\zeta} \rightarrow 0$ for $\omega \rightarrow \infty$) and for vanishing volume viscosity ($\zeta = 0$). This shows that compression effects dominate at very high frequencies for constant volume viscosity. Remarkably, the friction functions in the frequency domain differ only marginally for frequency-dependent and vanishing volume viscosity over the entire frequency domain (see Appendix N), which demonstrates that earlier assumptions of the Stokes hypothesis [40], i.e. the neglect of volume viscosities, are a reasonable approximation. The friction depends on the slip length b . As $\omega \rightarrow 0$ and for small radii, the real part goes to $6\pi\eta_0a$ for $\hat{b} \rightarrow 0$ and to $4\pi\eta_0a$ for $\hat{b} \rightarrow \infty$, as indicated by horizontal lines in fig. 4, and as expected [33]. The imaginary part of the friction functions for large radii does not decay to zero as $\omega \rightarrow \infty$ but reaches a plateau. In Appendix N, we discuss the asymptotic behavior of

the friction function for low and high frequencies, in dependence of the volume viscosity. In Appendix O, we investigate the influence of the decay constants α^{-1} and λ^{-1} and find a non-negligible influence of the decay constants in radii ranges of single water molecules.

D. Comparison of the Hydrodynamic and GLE Friction Functions

We compare the time-dependent friction of a single water molecule in liquid water from the GLE in Eq. 12 and the hydrodynamic prediction in Eq. 8. In fig. 5 (A), we show the extracted friction $\Gamma(t)$, obtained by the extraction technique described in Appendix E, which is the same result as in fig. 1. In fig. 5 (B), we show the real part of the friction in the frequency domain $\tilde{\Gamma}_+(\omega)$ (black). The friction obtained from single-particle trajectories includes the same features as the hydrodynamic prediction for the friction (green), obtained from Eq. 8. Especially, a dominant peak around 6-8 THz is visible in both func-

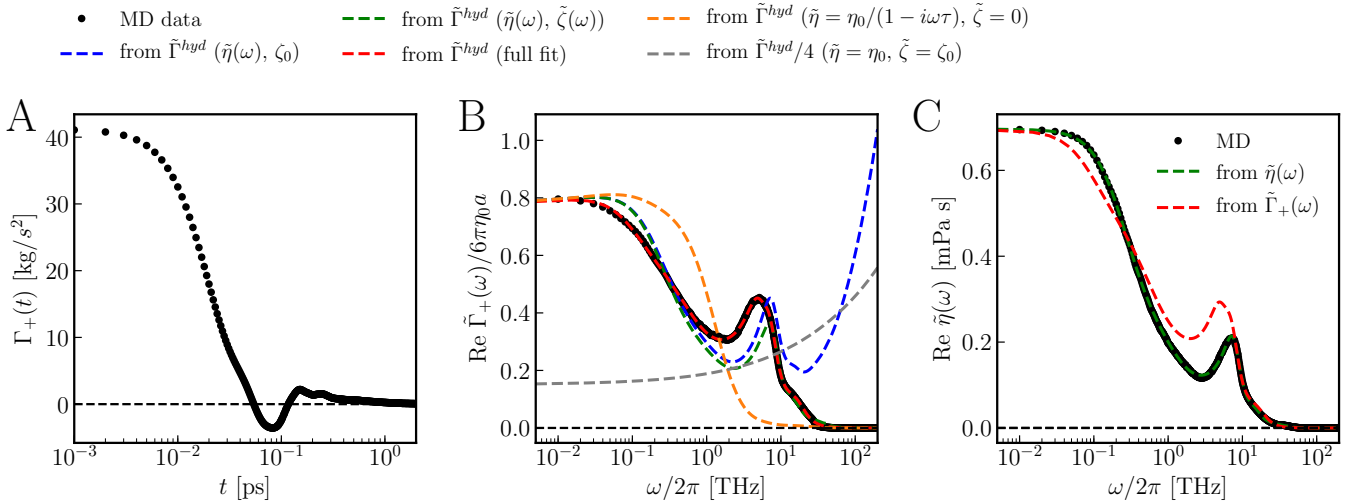


FIG. 5. A: Extracted memory kernel $\Gamma(t)$ from the SPC/E water model MD simulation (same as fig. 1). B: Real part of the Fourier transformed friction computed directly from (A). We compare the computed friction with the results from the friction function in Eq. 8 for $a = 150.14$ pm and $\hat{b} = b/a = 0.67$ and the shear viscosity parameters from tab. II (Appendix H). We obtain the values for a and b from fits to the MD results in frequency domain (black). We compare the friction with constant volume viscosity $\zeta_0 = \sum_j \zeta_{0,j} = 1.69$ mPa s (blue) and the fitted viscoelastic model $\tilde{\zeta}(\omega)$ in fig. 3 (green). Additionally, we show the friction with an adjusted fit in Eq. 8 (red). Here, we keep the volume viscosity ζ to the values in tab. III and adjust the shear viscosity. The resulting time scales and steady-state shear viscosities of the fit are listed in tab. IV (Appendix H). The grey line represents the friction with constant shear viscosity $\eta_0 = \sum_j \eta_{0,j} = 0.70$ mPa s and volume viscosity $\zeta_0 = \sum_j \zeta_{0,j} = 1.69$ mPa s. The orange line shows the friction using a single exponential-oscillatory model fit for the shear viscosity and vanishing volume viscosity. The fitting constants are $\eta_0 = 0.70$ mPa s, $(2\pi \cdot \tau_n)^{-1} = 3.33$ THz and $(2\pi \cdot \tau_o)^{-1} = 1.69$ THz. C: The real part of the MD data shear viscosity spectra from fig. 2 (B) compared with a fit into this data (green, Eq. 18) with the fitting constants in tab. II and the time scales adjusted to the friction (red line in (B), tab. IV).

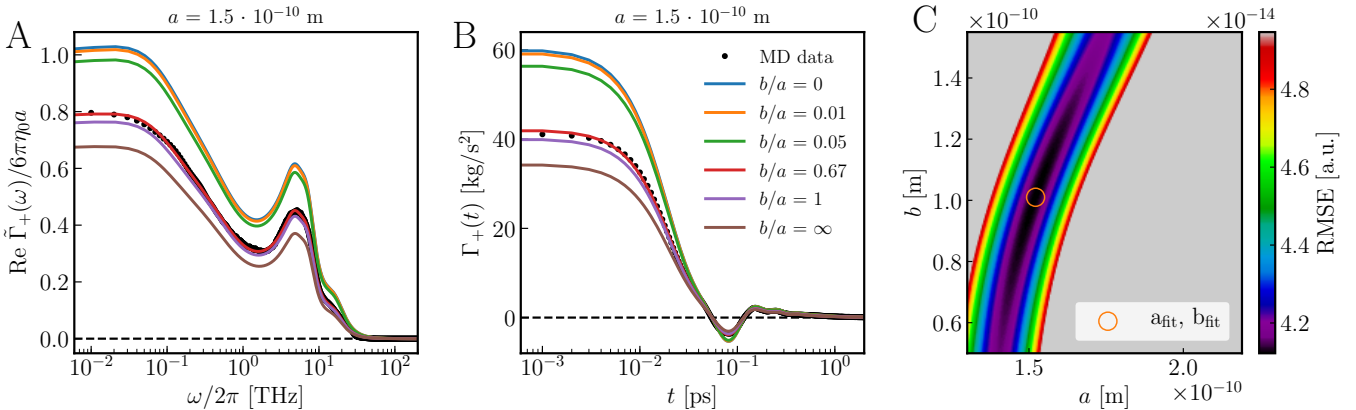


FIG. 6. A: Real part of the friction function $\text{Re } \tilde{\Gamma}_+(\omega)$ in fig. 5 (B, red line) in dependence of the slip coefficient $\hat{b} = b/a$, with fixed radius $a = 1.5 \cdot 10^{-10}$ m. B: Results of (A) in time domain. C: Root mean squared error (RMSE) between the MD data of the real part of the friction $\text{Re } \tilde{\Gamma}_+(\omega)$ in fig. 5 (B, black), and the fit into the data using Eq. 8 in dependence of the sphere radius a and the slip length b . The orange circle denote the optimal parameter combination for the result in fig. 5 (B).

tions. Here, we use $a = 150.14$ pm and $\hat{b} = 0.67$, which we obtain from fitting the MD results in frequency domain (black).

We compare the friction with constant volume viscosity $\zeta_0 = \sum_j \zeta_{0,j} = 1.69$ mPa s (blue) and the frequency-dependent function $\tilde{\zeta}(\omega)$ in fig. 3 (green). As explained in

fig. 4, a frequency-independent volume viscosity does not reproduce the correct high-frequency behavior. The prediction using the frequency-dependent shear and volume viscosities agrees rather nicely with the friction function directly extracted from the GLE, though. The dominant peak in the friction is slightly shifted. Additionally, in fig. 5 (B) we show the friction with an adjusted fit of

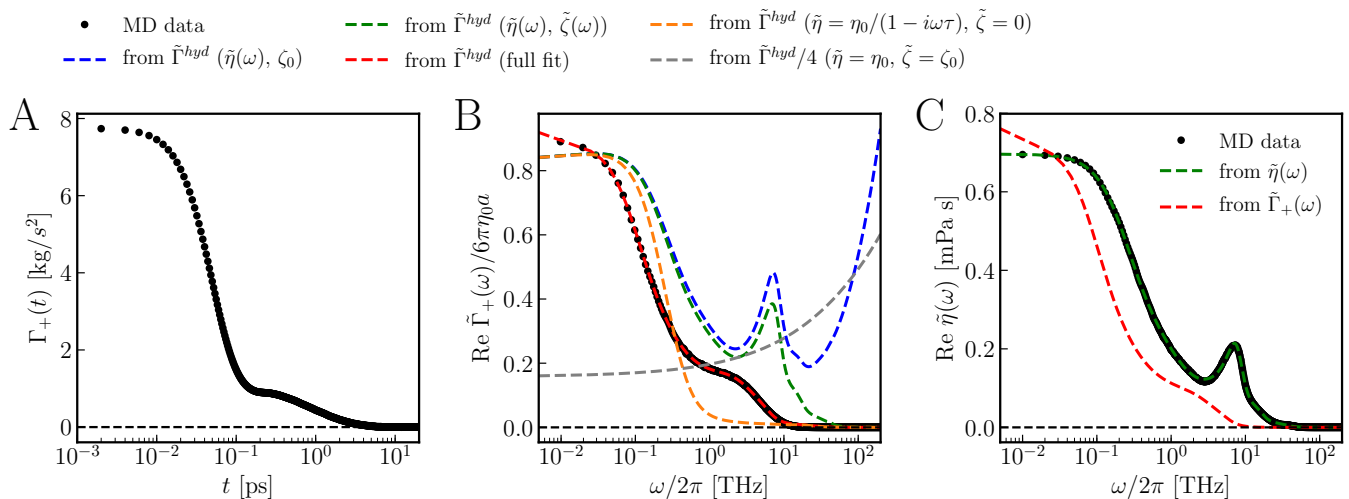


FIG. 7. A: Extracted memory kernel $\Gamma(t)$ from a SPC/E water model MD simulation of a methane molecule in water (time resolution 2 fs, data from [8]). B: Real part of the Fourier transformed friction computed directly from (A). We compare the computed friction with the results from the friction function in Eq. 8 for $a = 139.29$ pm and $\hat{b} = 0.36$ and the shear viscosity parameters from tab. II (Appendix H). We compare the friction functions with constant volume viscosity $\zeta_0 = \sum_j \zeta_{0,j} = 1.69$ mPa s (black) and the fitted viscoelastic model $\tilde{\zeta}(\omega)$ in fig. 3 (green). Additionally, we show the friction with an adjusted fit in Eq. 8 (red, same procedure as in fig. 5). The resulting time scales and steady-state shear viscosities of the fit are listed in tab. V (Appendix H). The grey line represents the stress response with constant shear viscosity $\eta_0 = \sum_j \eta_{0,j} = 0.70$ mPa s and volume viscosity $\zeta_0 = \sum_j \zeta_{0,j} = 1.69$ mPa s. The orange line shows the friction function using a single exponential-oscillatory model fit for the shear viscosity and vanishing volume viscosity. The fitting constants are $\eta_0 = 0.70$ mPa s, $(2\pi \cdot \tau_n)^{-1} = 0.67$ THz and $(2\pi \cdot \tau_o)^{-1} = 0.34$ THz. C: The real part of the MD data shear viscosity spectra from fig. 2 (B) compared with a fit into this data (green, Eq. 18) with the fitting constants in tab. II and the time scales adjusted to the memory kernel (red line in (B), tab. V).

the shear viscosity in Eq. 8 (red). For this, we perform a least-square fit of the MD data for $\text{Re } \tilde{\Gamma}_+(\omega)$, similar to the fitting procedure given in Appendix I. Here, we keep the volume viscosity ζ to the values in tab. III and adjust the shear viscosity, which is shown in fig. 5 (C) as a broken red line. The resulting times and steady shear viscosities of the fit are listed in tab. IV (Appendix H). The grey line in fig. 5 represents the friction with constant shear viscosity $\eta_0 = \sum_j \eta_{0,j} = 0.70$ mPa s and volume viscosity $\zeta_0 = \sum_j \zeta_{0,j} = 1.69$ mPa s, which demonstrates that frequency-dependent viscosities are needed to describe molecular friction in liquids. The orange line shows the friction using a single exponential-oscillatory model fit for the shear viscosity and vanishing volume viscosity, where we observe clear deviations between the data and the model. We thus see that the friction can be predicted very well, including complex shear and volume viscosity models, and the shear viscosity spectra can explain oscillations in the single-molecule friction function in the viscoelastic medium.

In fig. 5 (C) we show the real part of the MD data shear viscosity spectra from fig. 2 (B) compared with a fit of this data (green) with the fitting constants in tab. II and the time scales adjusted to the memory kernel (red line in fig. 5 (B)). Essentially this plot has the same message as fig. 5 (B). If we compute the shear viscosity from

the memory kernel itself, it again shows a slight deviation from the directly determined spectra from the stress tensor. We can conclude that there are two ways to determine the shear viscosity. One way is from the GLE in Eq. 14 and the other is from the Green-Kubo relation explained in Appendix M.

Interestingly, the good agreement for the low-frequency behavior in the friction function assumes non-negligible slip $b \neq 0$. The fitted values we obtained for the sphere radius $a = 150.14$ pm, and for the slip length $b = 100.99$ pm, are in realistic ranges of 1\AA . For a water molecule, the mass is $m = 3 \cdot 10^{-26}$ kg [8]. For a density of $\rho \approx 10^3$ kg/m³, the estimation of the hydrodynamic radius due to $m = \frac{4}{3}\pi\rho a^3$ is $a \approx 192.76$ pm, in good agreement with the estimated radius. The estimated radius and slip length are comparable with results of $a \approx 0.15$ nm and $b \approx 0.10$ nm presented by other authors [63], which they calculated by determining the translational and rotational diffusion constants for SPC/E water.

We show that we can estimate these parameters from MD simulations of single water molecules in a water reservoir via the memory kernel. In fig. 6, we investigate the dependence of the friction $\text{Re } \tilde{\Gamma}_+(\omega)$ on these parameters. We observe a dependence of the slip coefficient in fig. 6 (A), where higher slip leads to lower friction. The same is visible in the time domain in fig. 6 (B), obtained from (A). Here we applied the inverse Fourier transformation

on the real part of $\tilde{\Gamma}_+(\omega)$.

The slip length seems to have no major influence on the shape but predominantly on the magnitude of the friction function. In fig. 6 (C), we show the root mean squared error (RMSE) between the MD data of the real part of the friction $\text{Re } \tilde{\Gamma}_+(\omega)$ (fig. 5 (B, black), and the fit into the data using Eq. 8 in dependence of the sphere radius a and the slip coefficient b . We can find a global minimum, denoted as orange circle, which we use for the results in fig. 5 (B). We find that we can fit the effective radius much more accurately than the slip length.

E. Results for a Methane Molecule Moving in Water

In fig. 7 (A), we show the extracted memory kernel for a methane molecule in water, obtained by an MD simulation in SPC/E water. The data is taken from the work of Kowalik et al. [8]. The methane molecule in these simulations is modeled as a monoatomic Lennard-Jones sphere, which makes it possible to compute the friction using Eq. 8. In fig. 7 (B), we show the real part of the friction obtained from single-particle trajectories in the frequency domain (black). The friction does not show the same features as the prediction from the hydrodynamic equations (green). In particular, the pronounced oscillation peak at around 7-8 THz, arising from the shear viscosity of water, is absent. Here, we use $a = 139.29$ pm and $\tilde{b} = 0.36$, which we obtain from fits into the MD data (black). Again, we are able to adjust the shear viscosity for an accurate agreement between the friction functions (fig. 7 (B), red).

In fig. 7 (C), we observe deviations between a direct fit of the shear viscosity (green, Eq. 18) with the fitting constants in tab. II and the time scales adjusted to the friction (red line in (B), tab. V). This is to be expected since the memory kernel in fig. 7 (A) does not contain any noticeable oscillations, and all exponential-oscillatory components of the shear viscosity model are overdamped when adjusted to the friction from the single-particle memory kernel. This is visible by the fitted relaxation times in tab. V.

We observe considerable discrepancies between the friction from single-particle trajectories and the hydrodynamic prediction for a hydrophobic molecule in a water environment. Slip effects on the methane surface cannot explain these differences. Rather, the local shear viscosity near the methane molecule seems to differ from the bulk shear viscosity, which would explain the absence of the oscillation peak in the friction.

IV. CONCLUSIONS

We find that predictions from macroscopic hydrodynamic theory are in good agreement with the friction directly extracted from MD simulations of a single water

molecule in liquid water if the frequency-dependence of the shear and volume viscosities is properly accounted for. This establishes the link between the macroscopic fluid hydrodynamics and the microscopic molecular friction in a fluid. The results demonstrate that it is important to include the frequency-dependent volume viscosity of the fluid that has the asymptotic behavior $\tilde{\zeta} \rightarrow 0$ as $\omega \rightarrow \infty$. Interestingly, the agreement between the friction from the molecular water motion (obtained via the GLE) and the hydrodynamic prediction is obtained without including spatial or wave-vector dependencies of the viscosity functions. Nevertheless, we cannot exclude the possibility that such spatial dependencies are present, especially at high frequencies. We have mostly dealt with the homogeneous case where the moving molecule is identical to the surrounding fluid molecules. In contrast, we observe pronounced discrepancies between the friction obtained from hydrodynamic theory and from simulations for the inhomogeneous case of a methane molecule moving in water. We conclude that our current hydrodynamic model neglects the modified viscous properties of the water solvation layer around a methane molecule. It would therefore be desirable to develop inhomogeneous hydrodynamic models for the friction of host molecules in liquids in the presence of solvation shells that exhibit viscosity properties that are different from the bulk.

ACKNOWLEDGEMENTS

We gratefully acknowledge financial support from the Deutsche Forschungsgemeinschaft (DFG) via Grant SFB 1449, Project A02, and SFB 1114, Project C02.

APPENDIX

Appendix A: Derivation of the Friction of a Sphere from the Transient Stokes Equation

The Stokes equation in Eq. 6 is solved by calculating its Green's function [32, 35]. Taking the divergence of the Stokes equation in Eq. 6, we obtain

$$\begin{aligned} \nabla_i^2 P(\vec{r}, t) - \frac{\partial^2 P(\vec{r}, t)}{c^2 \partial t^2} = \nabla_i F_i(\vec{r}, t) \\ + \int \int \left[\frac{4}{3} \eta(|\vec{r}'|, t') + \zeta(|\vec{r}'|, t') \right] \nabla_i^2 \nabla_k v_k(\vec{r} - \vec{r}', t - t') d\vec{r}' dt', \end{aligned} \quad (\text{A1})$$

where we use the linearized continuity equation, i.e. $\rho_0 \nabla_i (\partial v_i / \partial t) = -\partial^2 \rho / \partial t^2$, and the definition of the compressibility, i.e. $\rho - \rho_0 = c^{-2} (P - P_0)$, from which, using the speed of sound c , follows $\partial^2 \rho / \partial t^2 = c^{-2} \partial^2 P / \partial t^2$.

We define the spatial and temporal Fourier transformation (FT) by

$$f(\vec{r}, t) = \frac{1}{(2\pi)^4} \int d\omega d^3k \tilde{f}(\vec{k}, \omega) e^{i(\vec{k} \cdot \vec{r} + \omega t)}. \quad (\text{A2})$$

Applying the FT in Eqs. 6 and A1, and using the rules of time and spatial convolution integrals, we obtain

$$i\omega\rho_0\tilde{v}_i(\vec{k},\omega)=\tilde{F}_i(\vec{k},\omega)-ik_i\tilde{P}(\vec{k},\omega) \quad (\text{A3})$$

$$-[\tilde{\eta}(\vec{k},\omega)/3+\tilde{\zeta}(\vec{k},\omega)]k_ik_j\tilde{v}_j(\vec{k},\omega)-\tilde{\eta}(\vec{k},\omega)k_jk_j\tilde{v}_i(\vec{k},\omega),$$

and

$$\left(\frac{\omega^2}{c^2}-k_ik_i\right)\tilde{P}(\vec{k},\omega)=ik_i\tilde{F}_i(\vec{k},\omega) \quad (\text{A4})$$

$$-i[4\tilde{\eta}(\vec{k},\omega)/3+\tilde{\zeta}(\vec{k},\omega)]k_ik_j\tilde{v}_j(\vec{k},\omega).$$

We assume that the viscosity kernels η and ζ are both single-sided in the time domain, i.e. $\eta(\vec{r},t)=0$ and $\zeta(\vec{r},t)=0$ for $t<0$. Furthermore, both viscosities are assumed to decay quickly in space, so that the Fourier transformation of the functions are independent of k , i.e. $\tilde{\eta}(\vec{k},\omega)\rightarrow\tilde{\eta}(\omega)$ and $\tilde{\zeta}(\vec{k},\omega)\rightarrow\tilde{\zeta}(\omega)$. Consequently, $\eta(\vec{r},t)$ and $\zeta(\vec{r},t)$ decay on a length scale much smaller than the length scale on which $\vec{\nabla}\vec{v}$ varies.

If we rearrange Eq. A4 for \tilde{P} and insert the expression in Eq. A3, we can eliminate \tilde{P} and arrive at an equation for the velocity as a function of the external force [32]. To solve this equation, we decompose the velocity into a transverse and a longitudinal part, i.e. $\tilde{v}_i(\vec{k},\omega)=\tilde{v}_i^T(\vec{k},\omega)+\tilde{v}_i^L(\vec{k},\omega)$, which fulfill $k_i\tilde{v}_i^T(\vec{k},\omega)=0$ and $k_i\tilde{v}_i^L(\vec{k},\omega)=k_i\tilde{v}_i^L(\vec{k},\omega)$. In Fourier space, the Green's function \tilde{G}_{ij} of the velocity is defined by

$$\tilde{v}_i(\vec{k},\omega)=\tilde{G}_{ij}(\vec{k},\omega)\tilde{F}_j(\vec{k},\omega), \quad (\text{A5})$$

and is a sum of transverse and longitudinal components, i.e. $\tilde{G}_{ij}(\vec{k},\omega)=\tilde{G}_{ij}^T(\vec{k},\omega)+\tilde{G}_{ij}^L(\vec{k},\omega)$. The transverse part describes the velocity field in the incompressible case and accounts for shear effects. It is given by

$$\tilde{G}_{ij}^T(\vec{k},\omega)=\frac{(\delta_{ij}-k_ik_j/k^2)/\tilde{\eta}(\omega)}{k^2+\alpha^2(\omega)}, \quad (\text{A6})$$

where the length scale α^{-1} is defined as

$$\alpha^2(\omega)=i\omega\rho_0/\tilde{\eta}(\omega). \quad (\text{A7})$$

The longitudinal component describes compression effects and reads

$$\tilde{G}_{ij}^L(\vec{k},\omega)=\frac{k_ik_j\lambda^2(\omega)}{\tilde{\eta}(\omega)\alpha^2(\omega)k^2(k^2+\lambda^2(\omega))}. \quad (\text{A8})$$

The length scale λ^{-1} is defined as

$$\lambda^2(\omega)=\frac{i\omega\rho_0}{4\tilde{\eta}(\omega)/3+\tilde{\zeta}(\omega)-i\rho_0c^2/\omega}. \quad (\text{A9})$$

The full frequency-dependent Green's function $G_{ij}(\vec{r},\omega)=G_{ij}^T(\vec{r},\omega)+G_{ij}^L(\vec{r},\omega)$ in real space reads

$$G_{ij}(\vec{r},\omega)=\frac{1}{4\pi\tilde{\eta}\alpha^2r^3}\{\delta_{ij}([1+r\alpha+r^2\alpha^2]e^{-r\alpha} \quad (\text{A10})$$

$$-[1+r\lambda]e^{-r\lambda})-3\hat{r}_i\hat{r}_j([1+r\alpha+r^2\alpha^2/3]e^{-r\alpha}$$

$$-[1+r\lambda+r^2\lambda^2/3]e^{-r\lambda})\}.$$

The asymptotic behavior of the Green's function strongly depends on the length scales $\alpha=\alpha(\omega)$ and $\lambda=\lambda(\omega)$, which is discussed in detail in [32]. Note that in [32] a different definition of the Fourier transformation is used, and constant viscosities are assumed.

To calculate the friction acting on an oscillating sphere, we have to compute the Green's function for the stress tensor, denoted by σ_{ijk} , defined as

$$\sigma_{ij}(\vec{r},\omega)=\sigma_{ijk}(\vec{r},\omega)F_k(\vec{r},\omega). \quad (\text{A11})$$

Without derivation and referring to [32], the stress tensor Green's function is given by

$$\sigma_{ijk}(\vec{r},\omega)/\tilde{\eta}(\omega)=G_{ijk}(\vec{r},\omega)+G_{jik}(\vec{r},\omega) \quad (\text{A12})$$

$$+(\alpha^2/\lambda^2-2)G_{llk}(\vec{r},\omega)\delta_{ij},$$

where $\nabla_k G_{ij}=G_{kij}$. To obtain the fluid velocity around a sphere with radius a , we use a standard singularity ansatz [35]

$$G_{ij}^{sp}(\vec{r},\omega)=(C_0+C_2a^2\nabla_k\nabla_k)G_{ij}(\vec{r},\omega), \quad (\text{A13})$$

where the velocity field around the sphere follows as $\tilde{v}_i^{sp}(\vec{r},\omega)=\tilde{F}_j(\omega)G_{ij}^{sp}(\vec{r},\omega)$, with \tilde{F}_j being a force source. We choose the coefficients C_0 and C_2 such that the boundary conditions on the spherical surface are satisfied. If we assume a finite slip at the spherical surface, we can split the boundaries at the surface into a kinematic and a Navier boundary condition. The kinematic boundary condition at $|r|=a$ can be written as

$$6\pi\tilde{\eta}(\omega)a\hat{r}_iG_{ij}^{sp}(\omega)=\hat{r}_j, \quad (\text{A14})$$

which defines the sphere velocity $\tilde{V}_i^{sp}(\omega)=\tilde{F}_i(\omega)/6\pi\tilde{\eta}(\omega)a$. Note that only in the zero-frequency limit, the source force $\tilde{F}_i(\omega)$ equals the actual force on the sphere. The Navier boundary condition for the tangential stress at $|r|=a$ reads

$$b[\nabla_kG_{ij}^{sp}(\omega)+\nabla_iG_{kj}^{sp}(\omega)]\hat{r}_k\mathcal{L}_i$$

$$=[G_{ij}^{sp}(\omega)-\delta_{ij}/6\pi\tilde{\eta}(\omega)a]\mathcal{L}_i, \quad (\text{A15})$$

where b is the slip length and we define the projection operator as $\mathcal{L}_i=(\delta_{li}-\hat{r}_l\hat{r}_i)$. The final result for $G_{ij}^{sp}(\vec{r},\omega)$ reads, using Eq. A10

$$G_{ij}^{sp}(\vec{r},\omega)=\frac{1}{4\pi\tilde{\eta}(\omega)\alpha^2r^3} \quad (\text{A16})$$

$$\cdot\left\{\delta_{ij}(E_1[1+r\alpha+r^2\alpha^2]e^{-r\alpha}-E_2[1+r\lambda]e^{-r\lambda})\right.$$

$$-3\hat{r}_i\hat{r}_j(E_1[1+r\alpha+r^2\alpha^2/3]e^{-r\alpha}$$

$$\left.-E_2[1+r\lambda+r^2\lambda^2/3]e^{-r\lambda})\right\},$$

with the coefficients

$$E_1=\frac{2}{3}e^{\hat{\alpha}}\frac{(1+2\hat{b})(3+3\hat{\lambda}+\hat{\lambda}^2)}{W}, \quad (\text{A17})$$

$$E_2=\frac{2}{3}e^{\hat{\lambda}}\frac{(1+2\hat{b})(3+3\hat{\alpha}+\hat{\alpha}^2)+\hat{b}\hat{\alpha}^2(1+\hat{\alpha})}{W}, \quad (\text{A18})$$

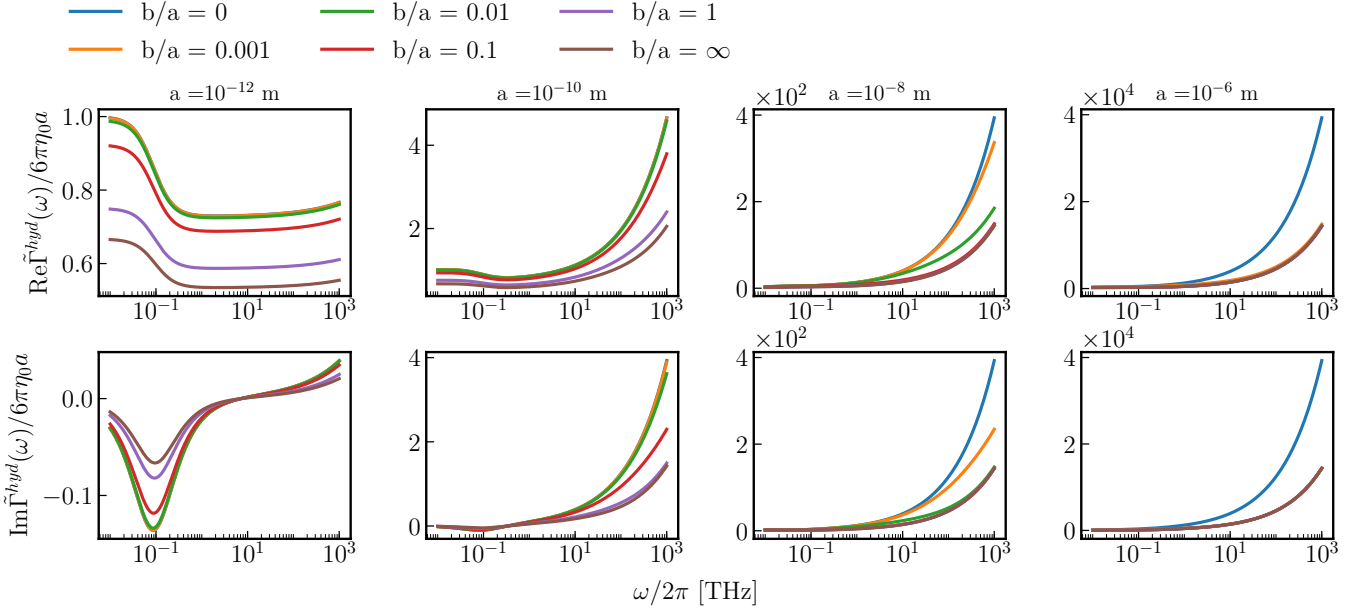


FIG. 8. Real and imaginary parts of the rescaled friction function of a sphere $\tilde{\Gamma}^{hyd}(\omega) = \text{Re} \Gamma^{hyd}(\omega) + i \text{Im} \Gamma^{hyd}(\omega)$ given by Eq. 8 for various normalized slip lengths \hat{b} and in dependence of the sphere radius a . Here we use a constant shear viscosity of $\eta_0 = 1$ mPa s, the water density $\rho = 10^3$ kg/m³, $c = 10^3$ m/s, and vanishing volume viscosity $\zeta = 0$ for comparability with [32].

and

$$W = (2 + 2\hat{\lambda} + \hat{\lambda}^2)(1 + \hat{b}(3 + \hat{\alpha})) + (1 + \hat{\alpha})(1 + 2\hat{b})\hat{\lambda}^2/\hat{\alpha}^2. \quad (\text{A19})$$

We define the dimensionless slip length, $\hat{b} = b/a$, and the dimensionless decay constants $\hat{\alpha} = a\alpha$ and $\hat{\lambda} = a\lambda$. The corresponding friction function $\tilde{\Gamma}^{hyd}(\omega)$ is given by

$$\delta_{ij} \tilde{\Gamma}^{hyd}(\omega) = \frac{\tilde{F}_i^{sp}(\omega)}{\tilde{V}_j^{sp}(\omega)} = -6\pi\tilde{\eta}(\omega)a \int d^3r \hat{r}_k \sigma_{kij} \delta(|r| - a), \quad (\text{A20})$$

where \tilde{V}_j^{sp} is the frequency-dependent velocity amplitude of the sphere. For the hydrodynamic force $\tilde{F}_i^{sp}(\omega)$ on a spherical particle, we use the projection of the stress tensor on the surface and integrate over the sphere surface. Using Eq. A12, and the derivative of $G_{ij}^{sp}(\vec{r}, \omega)$ in Eq. A16, we obtain the friction function of the spherical particle

$$\tilde{\Gamma}^{hyd}(\omega) = \frac{4\pi\tilde{\eta}(\omega)a}{3} W^{-1} \{ (1 + \hat{\lambda})(9 + 9\hat{\alpha} + \hat{\alpha}^2)(1 + 2\hat{b}) + (1 + \hat{\alpha})[2\hat{\lambda}^2(1 + 2\hat{b}) + \hat{b}\hat{\alpha}^2(1 + \hat{\lambda})] \}, \quad (\text{A21})$$

where we use the identities $\int d^3r \delta_{ij} \delta(|r| - a) = 4\pi a^2 \delta_{ij}$ and $\int d^3r \hat{r}_i \hat{r}_j \delta(|r| - a) = 4\pi a^2 \delta_{ij}/3$. Assuming negligible slip, i.e. $b \rightarrow 0$, and vanishing compressibility, i.e. $\lambda \rightarrow 0$, we have

$$\tilde{\Gamma}^{hyd}(\omega) = 6\pi a \tilde{\eta}(\omega) (1 + a\alpha + a^2\alpha^2/9). \quad (\text{A22})$$

Thus the frequency-dependent hydrodynamic force on a spherical particle $\tilde{F}_i^{sp}(\omega)$ (see Eq. A13) is given by

$$\tilde{F}_i^{sp}(\omega) = -6\pi a \tilde{\eta}(\omega) \tilde{V}_i^{sp}(\omega) (1 + a\alpha + a^2\alpha^2/9). \quad (\text{A23})$$

Applying the inverse Fourier transformation leads to, assuming frequency-independent shear viscosity [35],

$$F_i^{sp}(t) = -6\pi a \eta V_i^{sp}(t) - 6a^2 \sqrt{\pi \eta \rho_0} \int_{-\infty}^t dt' \frac{\dot{V}_i^{sp}(t')}{\sqrt{t-t'}} - \frac{2}{3} \pi \rho_0 a^3 \dot{V}_i^{sp}(t). \quad (\text{A24})$$

The first term in Eq. A24 is the steady Stokes drag. The second term, including a convolution integral, describes the sphere's history of motion, also known as the Basset history force. The third term is known as the added mass term, where $m_0 = \frac{2}{3} \pi \rho_0 a^3$. It originates since the accelerating sphere in the unsteady flow must move or deflect some surrounding fluid volume as it moves through it.

Appendix B: Friction of a Sphere for Frequency-Independent Viscosities

In fig. 8, we show the calculated friction function of a sphere for constant shear viscosity $\tilde{\eta}(\omega) = \eta_0$ in dependence of the sphere radius a . Note that we use a vanishing volume viscosity $\zeta = 0$, for better comparability with the results in [32]. As already discussed in [32], the friction function sensitively depends on the slip length b . It has an increasing behavior for the real and imaginary part as $\omega \rightarrow \infty$. Note that the high-frequency behavior of the imaginary part differs from the results in [32], as we use

a different definition of the Fourier transform. We refer to [32] for a detailed discussion of these results, but note that the addition of frequency-dependent shear and volume viscosity significantly changes the friction function (see fig. 4).

Appendix C: Fluid Momentum around a Moving Sphere

From the velocity field, i.e. $\tilde{v}_i^{sp}(\vec{r}, \omega) = \tilde{F}_j(\vec{r}, \omega)G_{ij}^{sp}(\vec{r}, \omega)$, and the expression in Eq. A16, we can calculate the fluid momentum outside the moving sphere

$$\tilde{p}_i(\omega) = \rho_0 \int_{|r|>a} \tilde{v}_i^{sp}(\vec{r}, \omega) d^3r. \quad (C1)$$

We assume that the force source is oscillating along the x-direction, i.e. $\tilde{F}(\omega) = (\tilde{F}(\omega), 0, 0)^T$, so that the momentum points in the x-direction. The volume integral in Eq. C1 involves in the angular integrals

$$\begin{aligned} \int_{|r|>a} d^3r \delta_{ij} &= \int_a^\infty r^2 dr \int_0^\pi d\theta \sin\theta \int_0^{2\pi} d\Phi \delta_{ij}, \quad (C2) \\ &= 4\pi \delta_{ij} \int_a^\infty r^2 dr, \\ \int_{|r|>a} d^3r \hat{r}_i \hat{r}_j &= \int_a^\infty r^2 dr \int_0^\pi d\theta \sin\theta \cos^2\theta \int_0^{2\pi} d\Phi \delta_{ij}, \\ &= 2\pi \delta_{ij} \int_a^\infty r^2 dr \int_{-1}^1 du u^2 \\ &= \frac{4}{3}\pi \delta_{ij} \int_a^\infty r^2 dr. \quad (C3) \end{aligned}$$

In the derivation of the flow field around a sphere in Appendix A, we use the kinematic boundary condition, i.e. $6\pi a \tilde{\eta}_i G_{ij}^{sp} = \hat{r}_j$ for $|r| = a$, in Eqs. A14 and A15 and defined the sphere velocity $\tilde{V}_i^{sp}(\omega) = \tilde{F}_i(\omega)/6\pi\tilde{\eta}(\omega)a$ such that in the low-frequency (steady) limit and without slip, the source force equals the actual force on the sphere. Using this definition, the identities in Eq. C2 and the expression in Eq. A16 and inserting them into Eq. C1, we arrive at

$$\tilde{p}_i(\omega) = 6\pi \frac{\rho_0}{\alpha^2} a \tilde{V}_i^{sp}(\omega) \int_a^\infty \frac{1}{r} dr \quad (C4)$$

$$\cdot \left\{ \delta_{ij} (E_1 [1 + r\alpha + r^2\alpha^2] e^{-r\alpha} - E_2 [1 + r\lambda] e^{-r\lambda}) - \delta_{ij} (E_1 [1 + r\alpha + r^2\alpha^2/3] e^{-r\alpha} - E_2 [1 + r\lambda + r^2\lambda^2/3] e^{-r\lambda}) \right\},$$

$$= 6\pi \frac{\rho_0}{\alpha^2} a \tilde{V}_i^{sp}(\omega) \int_a^\infty dr \left[\frac{2}{3} E_1 r \alpha^2 e^{-r\alpha} + \frac{1}{3} E_2 r \lambda^2 e^{-r\lambda} \right], \quad (C5)$$

$$= -6\pi \frac{\rho_0}{\alpha^2} a \tilde{V}_i^{sp}(\omega) \left[\frac{2}{3} E_1 [e^{-r\alpha}(r\alpha + 1)] \Big|_a^\infty + \frac{1}{3} E_2 [e^{-r\lambda}(r\lambda + 1)] \Big|_a^\infty \right], \quad (C6)$$

$$= 6\pi \frac{\rho_0}{\alpha^2} a \tilde{V}_i^{sp}(\omega) \left[\frac{2}{3} E_1 [e^{-a\alpha}(a\alpha + 1)] + \frac{1}{3} E_2 [e^{-a\lambda}(a\lambda + 1)] \right], \quad (C7)$$

For $b \rightarrow 0$ and $\lambda \rightarrow 0$, the constants E_1 and E_2 in Eqs. A17 and A18 become $E_1 = e^{a\alpha}$ and $E_2 = (1 + a\alpha + a^2\alpha^2/3)$, and we obtain for the momentum

$$\tilde{p}_i(\omega) = 6\pi \frac{\rho_0}{\alpha^2} a \tilde{V}_i^{sp}(\omega) (1 + a\alpha + a^2\alpha^2/9). \quad (C8)$$

The force is given by $\tilde{F}_i = i\omega \tilde{p}_i$, which leads to

$$\tilde{F}_i(\omega) = 6\pi a \tilde{\eta}(\omega) \tilde{V}_i^{sp}(\omega) (1 + a\alpha + a^2\alpha^2/9), \quad (C9)$$

which is identical to the result obtained in Eq. C1 from integrating the surface force over the oscillating sphere. Thus, the net momentum of the fluid inside the sphere has to vanish, and we have no added mass due to the motion of the liquid inside the sphere. It follows that the friction $\tilde{\Gamma}^{hyd}$ calculated from hydrodynamic theory equals the friction $\Gamma(t)$ extracted from single-particle trajectories using the GLE and no fluid mass correction has to be applied.

Appendix D: Simulation Setup

We perform all MD simulations using the GROMACS simulation package [64] (version 2020-Modified). For water, we use the SPC/E [65] and TIP4P/2005 [66] rigid water models. We pre-equilibrated in an NPT ensemble using a Berendsen barostat [67] set to 1 atm. For production runs, we perform all simulations in the NVT ensemble with a temperature of 300 K, controlled with a velocity rescaling thermostat [68]. For electrostatics, we use the particle-mesh Ewald method [69], with a cut-off length of 1 nm. We allow simulations to run for 600 ns, using integration time steps of 1 fs. We perform simulations in a 3.5616 nm cubic box with 1250 water molecules. For the results we show in Appendix K, we additionally run simulations with integration time steps of 2 and 4 fs.

Appendix E: Calculation of the Frequency-Dependent Friction from Particle Trajectories

Various data-based methods to estimate the parameters of the GLE have been proposed [5, 10, 70–72]. A robust and computationally efficient technique to compute the memory kernel from given time series trajectories is provided by multiplying Eq. 12 with the initial velocity $\dot{x}(0)$. Taking the ensemble average leads to an equation involving correlation functions we can calculate from the

given trajectory [10, 73, 74]. We obtain a Volterra equation of the first kind

$$mC^{\dot{x}\dot{x}}(t) = -\int_0^t dt' \Gamma(t')C^{\dot{x}\dot{x}}(t-t'), \quad (\text{E1})$$

where $C^{\dot{x}\dot{x}}(t) = \langle \dot{x}(0)\dot{x}(t) \rangle$, and $C^{\dot{x}\dot{x}}(t) = \langle \dot{x}(0)\dot{x}(t) \rangle$, and we use that $\nabla U = 0$. We use the fact that $\dot{x}(0)$ and $F_R(t)$ are uncorrelated, i.e. $\langle \dot{x}(0)F_R(t) \rangle = 0$ [1].

Analyses for one-dimensional trajectories have shown that, compared to the direct method [10], extraction of the memory kernel's running integral produces significantly more stable results [8]. We integrate Eq. E1 over time

$$m(C^{\dot{x}\dot{x}}(t) - C^{\dot{x}\dot{x}}(0)) = -\int_0^t ds \int_0^s ds' \Gamma(s')C^{\dot{x}\dot{x}}(s-s'), \quad (\text{E2})$$

$$= -\int_0^t ds' \int_{s'}^t ds \Gamma(s-s')C^{\dot{x}\dot{x}}(s'), \quad (\text{E3})$$

$$= -\int_0^t ds' \int_0^{t-s'} du \Gamma(u)C^{\dot{x}\dot{x}}(s'), \quad (\text{E4})$$

$$= -\int_0^t ds G(t-s)C^{\dot{x}\dot{x}}(s), \quad (\text{E5})$$

where $G(t) = \int_0^t \Gamma(s) ds$ is the running integral of the memory kernel. Discretizing this equation with a time step Δt , we obtain an iterative formula for $G_i = G(i\Delta t)$. For a discretized correlation function we use the shorthand notation $C_i^{AB} = \langle A(0)B(i\Delta t) \rangle$. For the running integral of the memory kernel G_i , we obtain from Eq. E5 by applying the trapezoidal rule

$$G_i = \left[m(C_i^{\dot{x}\dot{x}} - C_0^{\dot{x}\dot{x}}) - \Delta t \sum_{j=1}^{i-1} G_j C_{i-j}^{\dot{x}\dot{x}} \right] \cdot \left(\frac{1}{2} \Delta t C_0^{\dot{x}\dot{x}} \right)^{-1}, \quad (\text{E6})$$

where we use $G_0 = 0$. If we compute the velocity autocorrelation function $C_i^{\dot{x}\dot{x}}$ from the given time series $x(t)$, we can use this Eq. E6 to determine the running integral $G(t)$ and based on this the memory kernel $\Gamma(t)$ by differentiation.

Appendix F: Derivation of Oscillating Memory Kernels from Coupled Degrees of Freedom

Memory effects arise from the coupling of the reaction coordinate $x(t)$ to auxiliary coordinates [75]. The Hamiltonian of the simplest system, where the dynamics of $x(t)$ with velocity $v(t) = \dot{x}(t)$ and mass m is linearly coupled to a coordinate $y(t)$ with velocity $w(t) = \dot{y}(t)$ and mass m_y is given by

$$H = \frac{m}{2}v^2 + \frac{m_y}{2}w^2 + \frac{k}{2}(x-y)^2 + U(x), \quad (\text{F1})$$

where k is the coupling constant. The Langevin equation of this Hamiltonian reads [76–78]

$$m\dot{v}(t) = -k[x(t) - y(t)] - \nabla U(x), \quad (\text{F2})$$

$$m_y\dot{w}(t) = -\gamma_y w(t) + k[x(t) - y(t)] + F_y(t), \quad (\text{F3})$$

where $F_y(t)$ is a stationary Gaussian process with zero mean, i.e. $\langle F_y(t) \rangle = 0$, and strength $\langle F_y(t)F_y(t') \rangle = 2\gamma_y k_B T \delta(t-t')$. This set of coupled differential equations in Eqs. F2 and F3 is equivalent to the generalized Langevin equation in Eq. 12 where the memory kernel $\Gamma(t)$ has the form of an exponential-oscillatory kernel in Eq. 15. To show this, we solve the equation for the variable $y(t)$

$$y(t) = x(t) - \int_{-\infty}^t dt' v(t') e^{-(t-t')/(2\tau_n)} \cdot \left[\cosh(\omega_*(t-t')) + \frac{1}{2\tau_n\omega_*} \sinh(\omega_*(t-t')) \right] - \int_{-\infty}^t dt' F_y(t') e^{-(t-t')/(2\tau_n)} \frac{1}{\tau_o^2\omega_*} \sinh(\omega_*(t-t')), \quad (\text{F4})$$

where we define the time scales $\tau_n = m_y/\gamma_y$ and $\tau_o = \sqrt{m_y/k}$, and the frequency $\omega_* = \sqrt{(2\tau_n)^{-2} - (\tau_o)^{-2}}$. If we insert Eq. F4 into Eq. F2 and replace $t' \rightarrow t-t'$, we arrive at

$$m\dot{v}(t) = -\int_{-\infty}^{\infty} dt' \Gamma(t')v(t-t') + F_R(t) - \nabla U(x). \quad (\text{F5})$$

This is the standard generalized Langevin equation with given memory kernel and random force

$$\Gamma_+(t) = \Theta(t) \left\{ k e^{-\frac{t}{2\tau_n}} \left[\cosh(\omega_* t) + \frac{1}{2\tau_n\omega_*} \sinh(\omega_* t) \right] \right\}, \quad (\text{F6})$$

$$F_R(t) = \frac{1}{\tau_o^2\omega_*} \int_{-\infty}^{\infty} dt' F_y(t') e^{-(t-t')/(2\tau_n)} \sinh(\omega_*(t-t')). \quad (\text{F7})$$

One can show that $F_R(t)$ follows a stationary Gaussian process with $\langle F_R(t) \rangle = 0$ and $\langle F_R(t)F_R(t') \rangle = k_B T \Gamma(|t-t'|)$, which confirms the equivalence between the GLE and the Markovian system. The memory kernel in Eq. F6 can be rewritten by defining $\omega_* = i\frac{1}{2\tau_n}\kappa$, with $\kappa = \sqrt{4(\tau_n/\tau_o)^2 - 1}$, and we obtain the exponential-oscillating memory kernel in the form of Eq. 15.

Appendix G: Mass-Less Limit of the Exponential-Oscillatory Memory Kernel

We start from the expression of the exponential-oscillatory memory kernel in Eq. F6. Defining the oscillation time $\tau_* = i/\omega_*$, the two-sided memory kernel

reads

$$\Gamma(t) = \frac{k}{2} e^{-\frac{t}{2\tau_n}} \left[e^{it/\tau_*} + e^{-it/\tau_*} + \frac{\tau_*}{2\tau_n} \left(e^{it/\tau_*} - e^{-it/\tau_*} \right) \right], \quad (\text{G1})$$

$$= k e^{-\frac{t}{2\tau_n}} \left[\cos\left(t/\tau_*\right) + \frac{\tau_*}{2\tau_n} \sin\left(t/\tau_*\right) \right]. \quad (\text{G2})$$

Using $\tau_n = m_y/\gamma_y$, $\tau_o = \sqrt{m_y/k}$, and $\omega_* = \sqrt{(2\tau_n)^{-2} - (\tau_o)^{-2}}$, the oscillation time τ_* can be written as

$$\tau_* = \left(\frac{k}{m_y} - \frac{\gamma_0^2}{4m_y^2} \right)^{-1/2} = i \frac{2m_y}{\gamma_0} \left(1 - \frac{4m_y k}{\gamma_0^2} \right)^{-1/2}. \quad (\text{G3})$$

Taking $m_y \rightarrow 0$, we obtain $\tau_* \approx i \frac{2m_y}{\gamma_0} = i2\tau_n$. Using the Taylor series of $\sqrt{1-x} \approx 1 - x/2$, $1/\tau_*$ for $m_y \rightarrow 0$ is approximated as

$$\lim_{m_y \rightarrow 0} \frac{1}{\tau_*} \approx -i \frac{\gamma_0}{2m_y} \left(1 - \frac{2km_y}{\gamma_0^2} \right) \approx -\frac{i}{2\tau_n} + \frac{ik}{\gamma_0}. \quad (\text{G4})$$

With the limits for τ_* and $1/\tau_*$, we find that the massless limit of the memory kernel in Eq. G1 is a single-exponential function

$$\lim_{m_y \rightarrow 0} \Gamma(t) \approx k e^{-tk/\gamma_0} = k e^{-t/\tau}, \quad (\text{G5})$$

where we define the memory time $\tau = \gamma_0/k$. The single-exponential memory kernel, i.e. $\Gamma_+(t) = \Theta(t)(\gamma_0/\tau)e^{-t/\tau}$ can be transformed to frequency space and reads

$$\tilde{\Gamma}_+(\omega) = \frac{\gamma_0}{1 - i\omega\tau}. \quad (\text{G6})$$

Appendix H: Summary of Fitting Parameters

TABLE I. Fitting parameters for the model memory kernel in Eqs. 15, 16 of the SPC/E and the TIP4P/2005 water model. The time scales are converted to frequencies for ease of comparison with fig. 1 (E, F).

Parameter	SPC/E	TIP4P/2005
$\gamma_{0,I}$	$5.57 \cdot 10^{-13}$ kg/s	$1.51 \cdot 10^{-12}$ kg/s
$(2\pi \cdot \tau_{n,I})^{-1}$	3.92 THz	20.39 THz
$(2\pi \cdot \tau_{o,I})^{-1}$	1.32 THz	19.36 THz
$\gamma_{0,II}$	$1.04 \cdot 10^{-13}$ kg/s	$2.31 \cdot 10^{-12}$ kg/s
$(2\pi \cdot \tau_{n,II})^{-1}$	3.11 THz	4.61 THz
$(2\pi \cdot \tau_{o,II})^{-1}$	4.75 THz	6.96 THz
$\gamma_{0,III}$	$2.55 \cdot 10^{-13}$ kg/s	$1.27 \cdot 10^{-13}$ kg/s
$(2\pi \cdot \tau_{n,III})^{-1}$	5.39 THz	2.71 THz
$(2\pi \cdot \tau_{o,III})^{-1}$	7.45 THz	4.56 THz
$\gamma_{0,IV}$	$1.37 \cdot 10^{-13}$ kg/s	$9.11 \cdot 10^{-13}$ kg/s
$(2\pi \cdot \tau_{n,IV})^{-1}$	18.30 THz	31.37 THz
$(2\pi \cdot \tau_{o,IV})^{-1}$	18.65 THz	2.13 THz
$\gamma_{0,V}$	$4.34 \cdot 10^{-13}$ kg/s	$3.46 \cdot 10^{-13}$ kg/s
$(2\pi \cdot \tau_{n,V})^{-1}$	3.53 THz	1.16 THz
$(2\pi \cdot \tau_{o,V})^{-1}$	0.65 THz	0.72 THz

TABLE II. Fitting parameters for the viscoelastic model of the shear viscosity in Eqs. 17, 18 to MD data of the SPC/E water model and the TIP4P/2005 water model. The time scales are converted to frequencies for ease of comparison with fig. 2 (E, F).

Parameter	SPC/E	TIP4P/2005
$\eta_{0,I}$	0.45 mPa s	0.25 mPa s
$(2\pi \cdot \tau_{n,I})^{-1}$	1.96 THz	1.83 THz
$(2\pi \cdot \tau_{o,I})^{-1}$	0.67 THz	0.47 THz
$\eta_{0,II}$	0.14 mPa s	0.06 mPa s
$(2\pi \cdot \tau_{n,II})^{-1}$	3.33 THz	1.94 THz
$(2\pi \cdot \tau_{o,II})^{-1}$	1.69 THz	1.54 THz
$\eta_{0,III}$	0.08 mPa s	0.06 mPa s
$(2\pi \cdot \tau_{n,III})^{-1}$	5.45 THz	4.16 THz
$(2\pi \cdot \tau_{o,III})^{-1}$	8.08 THz	7.74 THz
$\eta_{0,IV}$	0.02 mPa s	0.43 mPa s
$(2\pi \cdot \tau_{n,IV})^{-1}$	10.58 THz	2.04 THz
$(2\pi \cdot \tau_{o,IV})^{-1}$	15.50 THz	0.76 THz
$\eta_{0,V}$	0.005 mPa s	0.02 mPa s
$(2\pi \cdot \tau_{n,V})^{-1}$	27.47 THz	20.95 THz
$(2\pi \cdot \tau_{o,V})^{-1}$	31.74 THz	17.03 THz
$\eta_{0,VI}$	$3.31 \cdot 10^{-5}$ mPa s	$8.11 \cdot 10^{-4}$ mPa s
$(2\pi \cdot \tau_{n,VI})^{-1}$	6.31 THz	15.61 THz
$(2\pi \cdot \tau_{o,VI})^{-1}$	42.10 THz	39.73 THz

Appendix I: Fitting of the Extracted Memory Kernel and Viscosity Data

First, we fit the real part of the Fourier-transformed memory kernel $\tilde{\Gamma}_+(\omega)$ extracted from the MD simulation by a combination of five exponential-oscillating memory kernels according to Eq. 16. We thereby fit the input data in the parameter space using the Levenberg-Marquardt algorithm implemented in `scipy` v. 1.4 [79]. The initial values for all $\gamma_{0,j}$, $\tau_{n,j}$ and $\tau_{o,j}$ are chosen suitably. We

TABLE III. Fitting parameters for the viscoelastic model of the volume viscosity in Eqs. 20, 21 to MD data of the SPC/E water model and the TIP4P/2005 water model. The time scales are converted to frequencies for ease of comparison with fig. 3 (E, F).

Parameter	SPC/E	TIP4P/2005
$\zeta_{0,I}$	0.75 mPa s	0.23 mPa s
$(2\pi \cdot \tau_{v,I})^{-1}$	1.11 THz	0.13 THz
$(2\pi \cdot \tau_{w,I})^{-1}$	0.41 THz	0.09 THz
$\zeta_{0,II}$	0.45 mPa s	1.23 mPa s
$(2\pi \cdot \tau_{v,II})^{-1}$	1.53 THz	1.14 THz
$(2\pi \cdot \tau_{w,II})^{-1}$	0.75 THz	0.50 THz
$\zeta_{0,III}$	0.04 mPa s	0.01 mPa s
$(2\pi \cdot \tau_{v,III})^{-1}$	6.89 THz	4.33 THz
$(2\pi \cdot \tau_{w,III})^{-1}$	7.07 THz	7.10 THz
$\zeta_{0,IV}$	0.44 mPa s	0.55 mPa s
$(2\pi \cdot \tau_{v,IV})^{-1}$	5.52 THz	7.96 THz
$(2\pi \cdot \tau_{w,IV})^{-1}$	3.55 THz	4.14 THz
$\zeta_{0,V}$	0.02 mPa s	0.02 mPa s
$(2\pi \cdot \tau_{v,V})^{-1}$	20.76 THz	19.39 THz
$(2\pi \cdot \tau_{w,V})^{-1}$	18.20 THz	17.88 THz

TABLE IV. Resulting relaxation times and steady-state viscosities for the fit of the friction function in fig. 5 (red line in B).

Parameter	
$\eta_{0,I}$	0.32 mPa s
$(2\pi \cdot \tau_{n,I})^{-1}$	9.45 THz
$(2\pi \cdot \tau_{o,I})^{-1}$	2.29 THz
$\eta_{0,II}$	0.05 mPa s
$(2\pi \cdot \tau_{n,II})^{-1}$	3.54 THz
$(2\pi \cdot \tau_{o,II})^{-1}$	5.07 THz
$\eta_{0,III}$	0.08 mPa s
$(2\pi \cdot \tau_{n,III})^{-1}$	5.22 THz
$(2\pi \cdot \tau_{o,III})^{-1}$	7.58 THz
$\eta_{0,IV}$	0.04 mPa s
$(2\pi \cdot \tau_{n,IV})^{-1}$	16.43 THz
$(2\pi \cdot \tau_{o,IV})^{-1}$	17.53 THz
$\eta_{0,V}$	0.21 mPa s
$(2\pi \cdot \tau_{n,V})^{-1}$	0.68 THz
$(2\pi \cdot \tau_{o,V})^{-1}$	0.24 THz
$\eta_{0,VI}$	0.07 mPa s
$(2\pi \cdot \tau_{n,VI})^{-1}$	0.01 THz
$(2\pi \cdot \tau_{o,VI})^{-1}$	0.0009 THz

constrain the parameter space to positive values. As input data, we filter the data set beforehand on logarithmic scale. We also weight the data exponentially, so that the data for small frequencies become more important for the fit. After optimizing the parameters, we use them as initial parameters for a fit of the data in the time domain. Here the input data are filtered again on logarithmic scale but without exponential weighting. This allows us to fit the low-frequency and high-frequency regimes very well at the same time. We repeat this procedure for finding the fit parameters according to Eqs. 18 and 21, for the

TABLE V. Resulting relaxation times and steady-state viscosities for the fit of the friction function in fig. 7 (red line in B) for the methane MD data [8].

Parameter	
$\eta_{0,I}$	0.53 mPa s
$(2\pi \cdot \tau_{n,I})^{-1}$	3.97 THz
$(2\pi \cdot \tau_{o,I})^{-1}$	0.63 THz
$\eta_{0,II}$	0.10 mPa s
$(2\pi \cdot \tau_{n,II})^{-1}$	4.42 THz
$(2\pi \cdot \tau_{o,II})^{-1}$	1.24 THz
$\eta_{0,III}$	0.08 mPa s
$(2\pi \cdot \tau_{n,III})^{-1}$	5.82 THz
$(2\pi \cdot \tau_{o,III})^{-1}$	3.59 THz
$\eta_{0,IV}$	0.02 mPa s
$(2\pi \cdot \tau_{n,IV})^{-1}$	5.35 THz
$(2\pi \cdot \tau_{o,IV})^{-1}$	5.39 THz
$\eta_{0,V}$	0.13 mPa s
$(2\pi \cdot \tau_{n,V})^{-1}$	2.70 THz
$(2\pi \cdot \tau_{o,V})^{-1}$	0.09 THz
$\eta_{0,VI}$	$3.31 \cdot 10^{-5}$ mPa s
$(2\pi \cdot \tau_{n,VI})^{-1}$	6.31 THz
$(2\pi \cdot \tau_{o,VI})^{-1}$	42.10 THz

MD data of the shear and volume viscosity respectively. The obtained fit parameters are summarized in tabs. I, II and III.

Appendix J: High-Frequency Scaling of the Memory Kernel

In fig. 9, we show the water memory kernel results in the high-frequency regime (same as fig. 1 but with logarithmic y-scales and for different x-scales), together with different functions for comparison. For high frequencies above 30 THz, the real part of the memory kernel in fig. 9 (A, B, C) decays much faster than $\sim 1/\omega^4\tau^4$ as follows from Eq. 16 or $\sim 1/\omega^2\tau^2$ (Eq. G6). In Appendix K, we show that this behavior also occurs at lower time resolutions of the MD simulation. In contrast, the imaginary part of the MD data decays with $\sim 1/\omega\tau$ (see dashed line in fig. 9 (D, E, F)), in agreement with Eqs. 16 and Eq. G6.

A discussion of the water memory kernel's real part in the high-frequency regime is given in [43]. There it was argued, justified by the smoothness of physical molecular trajectories for short times, that the memory kernel should decay exponentially for high frequencies, i.e. $\text{Re } \tilde{\Gamma}_+(\omega \rightarrow \infty) \sim (\omega\tau)^2 e^{-|\omega\tau|}$ (grey dashed line in fig. 9 (A, B, C)). This scaling behavior follows from a velocity autocorrelation function of the form $C_{vv}(t) = \langle v^2 \rangle [1 + (t/\tau)^2]^{-1}$ with $\langle v^2 \rangle = k_B T/m$ (see Appendix P). Since molecular trajectories are solutions of Newton's equations, they are smooth and include smooth velocity autocorrelation functions $C^{vv}(t)$, meaning that all derivatives of $C^{vv}(t)$ should exist at $t = 0$ and be finite. If we assume time-symmetric velocity autocorrelation func-

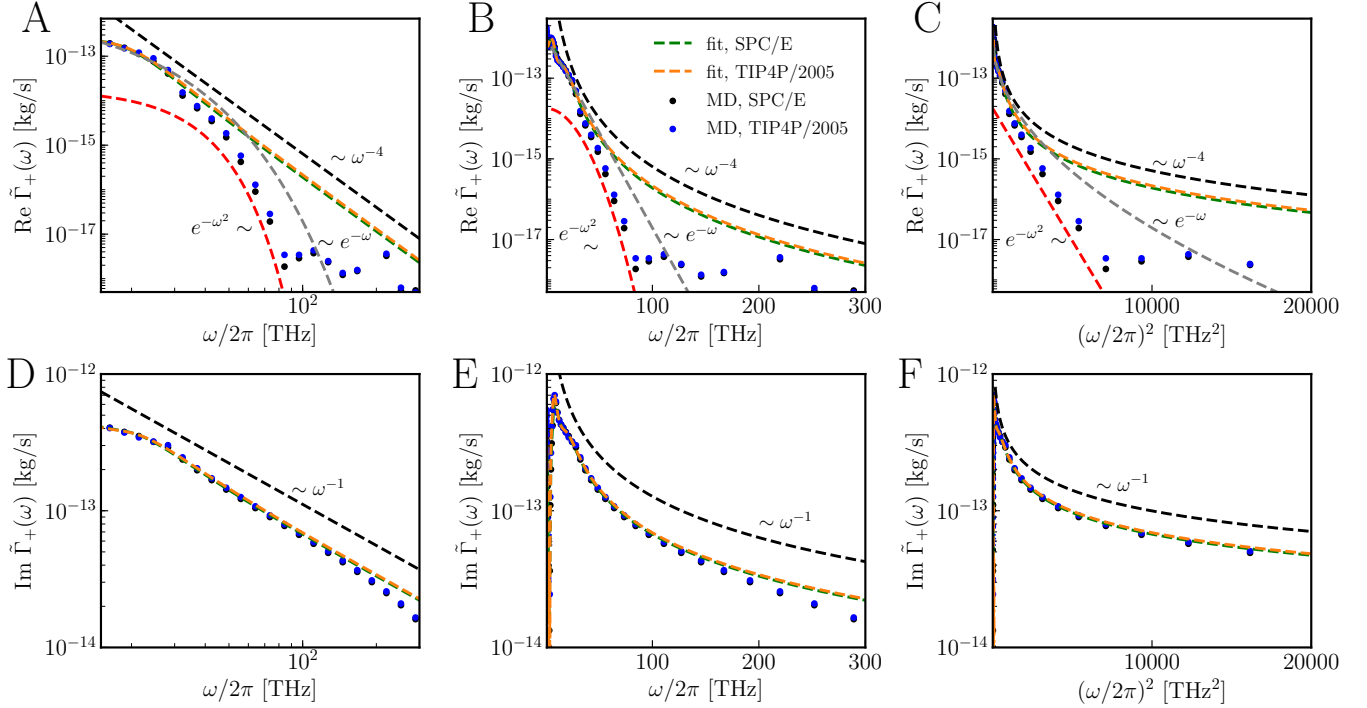


FIG. 9. High-frequency behavior of the complex memory kernel $\tilde{\Gamma}_+(\omega)$ of a single water molecule in water from MD simulations of SPC/E and TIP4P/2005 water with fits according to Eq. 16 and the fitting parameters in tab. I (Appendix H). We show scaling functions of the real part with an exponential-oscillatory model (black dashed line, Eq. 16), an exponential fast decay (grey dashed line) and a Gaussian memory kernel (red dashed line) for log-scaled x-axis (A), for linear-scaled x-axis (B) and for quadratic-scaled x-axis (C). The imaginary part in (D, E, F) scales well with $\sim 1/\omega\tau$. Note that the data is shown in logarithmic spacing for better visibility.

tions, i.e. $C^{vv}(t) = C^{vv}(-t)$, only even powers in t contribute in the short-time expansion. We investigate the short-time behavior of the exponential-oscillating memory kernel in Eq. F6 in Appendix Q and show that the memory kernel is non-analytic in the time domain. In Appendix R, we derive the resulting velocity autocorrelation function from an exponential-oscillatory kernel and find that not all derivatives exist in the short-time expansion.

In fig. 9 (A, B, C), we observe that the high-frequency behavior of the real part seems to be even better represented by a Gaussian memory kernel, i.e. $\Gamma(t) \sim e^{-t^2/\tau^2}$ or $\text{Re } \tilde{\Gamma}_+(\omega \rightarrow \infty) \sim e^{-\omega^2\tau^2}$ (red dashed line), which is visible by the quadratic x-axis in fig. 9 (C). In Appendix S, we show the origin of such a high-frequency scaling from a Gaussian-shaped velocity autocorrelation function. Although a Gaussian memory kernel seems to describe the data better than an exponential-oscillatory model, we can not identify a Markovian embedding for Gaussian memory kernels. Nevertheless, the good agreement between the MD data and the fits in fig. 9 for frequencies lower than 30 THz justifies our choice of a sum of exponential-oscillatory memory kernel components, which can be derived from coupled Hamiltonian dynamics (see Appendix F).

Appendix K: Friction from MD Simulations with Different Time Steps

In fig. 10, we investigate the influence of the time resolution of the MD simulation on the memory kernel, where we simulated SPC/E water for different time resolutions. Besides numerical noise, no distinct differences can be seen between the different time resolutions. All important features we observe in the memory kernel for 1 fs in fig. 1 are also visible at different time resolutions in fig. 10. The deviating behavior from the exponential-oscillatory fitting model starting around 30-60 THz which we see for 1 fs in fig. 9 (A, B, C) occurs at lower resolutions in fig. 10 (B), which rules out discretization problems in this frequency range. At higher frequencies, in the regime of the resolution limit, the data of the real part in fig. 10 (B) is dominated by noise, which means that we cannot make a statement about the actual high-frequency scaling. For the 1 fs data (black), the points become unstable around 100 THz, which is a fifth of the maximal frequency of 500 THz. This is also the regime where the imaginary part deviates from an expected ω^{-1} decrease (see fig. 10 (C)). This suggests that our used FFT algorithm is numerically unstable for the non-periodic data sets in this frequency regime, and data points in this regime should not be used for interpretation.

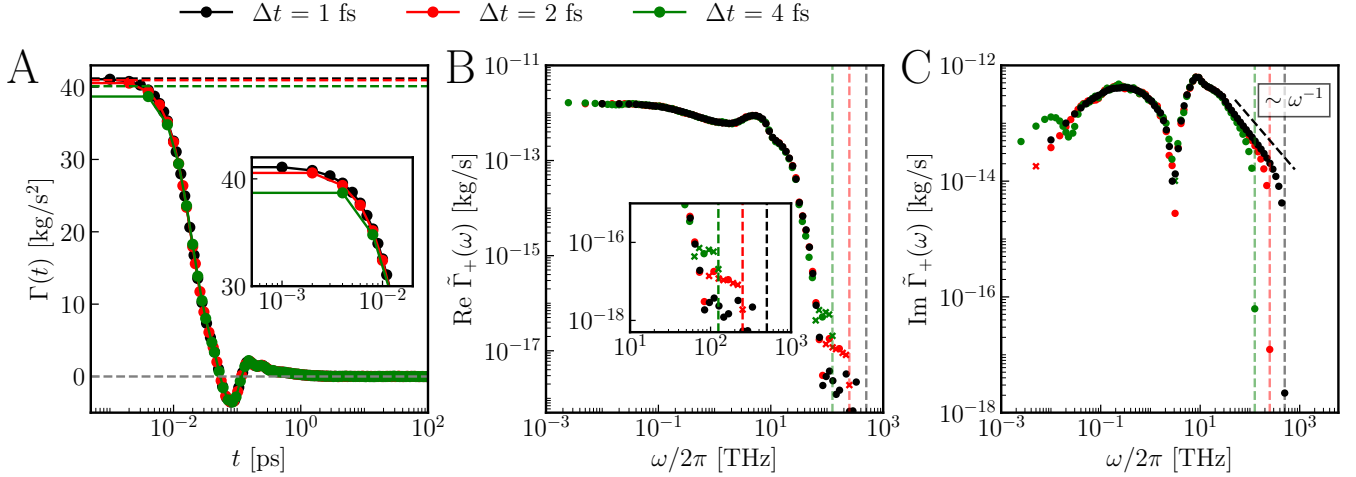


FIG. 10. Extracted water memory kernel $\Gamma(t)$ (A) and the real and imaginary part of the Fourier transformation $\tilde{\Gamma}_+(\omega)$ (B,C) for MD simulations (SPC/E) with different time resolutions. In the frequency domain, spheres denote positive values and x-points denote negative values. The colored dashed lines in the time domain (A) denote the initial values of the memory kernel data $\Gamma(0)$. The colored dashed lines in the frequency domain in (B,C) denote the maximal frequencies of the Fourier-transformed data.

Appendix L: Running Integral over the Friction Function

The friction coefficient of the memory kernel γ_0 can be obtained by the plateau value of the running integral over the memory kernel, i.e. $\gamma_0 = \int_0^\infty \Gamma(t) dt = G(t \rightarrow 0)$. In fig. 11, we show the running integrals $G(t) = \int_0^t \Gamma(t') dt'$ of the memory kernels in fig. 1, which we obtain by the extraction technique described in Appendix E. We estimate the plateau value of $G(t)$ via a fit with the function

$$G(t) = \sum_{i=1}^2 G_{0,i}(1 - e^{-t/\tau_i}) + G_{0,3}, \quad (\text{L1})$$

to the extracted running integral (see dashed lines in fig. 11). For the least-squares fit, we use the data in the time interval between 0.1 ps and 20 ps, since after 20 ps, the data is dominated by noise and we assume the plateau to be reached after 20 ps. The fits perfectly cover the plateaus in the data and we obtain friction coefficients of $\gamma_0 = G_{0,1} + G_{0,2} + G_{0,3} = 1.57$ kg/s for SPC/E water and 1.88 kg/s for TIP4P/2005 water, in agreement with the values obtained from the fits in the main text (see horizontal dashed lines in fig. 11).

Appendix M: Calculation of Frequency-Dependent Shear and Volume Viscosity Spectra from MD Simulations

The shear viscosity kernel $\eta(t)$ is given by the trace-free part of the stress tensor by the Green-Kubo relation

[2, 31, 36, 38]

$$\begin{aligned} \tilde{\eta}(\vec{k} = 0, \omega) &= \int_0^\infty e^{-i\omega t} \eta(t) dt, \\ &= \frac{V}{6k_B T} \int_0^\infty e^{-i\omega t} \sum_{i \neq j} \langle \Pi_{ij}(t) \Pi_{ij}(0) \rangle dt, \end{aligned} \quad (\text{M1})$$

where V is the volume of the fluid. We define the trace-free part of the stress tensor Π_{ij} as

$$\Pi_{ij} = \sigma_{ij} - \delta_{ij} \frac{1}{3} \sum_k \sigma_{kk}, \quad (\text{M2})$$

where $i, j \in \{x, y, z\}$. For the computation of the shear viscosity spectrum, we use Eq. M1 by calculating the time correlation functions of the stress tensor entries and applying the half-sided Fourier transform.

Employing the Green-Kubo relations, we use the fluctuations of the instantaneous pressure from its average value $\langle P \rangle$, i.e. $\delta P(t) = P(t) - \langle P \rangle$, to compute the volume viscosity kernel $\zeta(t)$. $P(t)$ is computed from the trace of the stress tensor, i.e. $P(t) = \frac{1}{3} \sum_k \sigma_{kk}(t)$. Using the half-sided Fourier transformation we compute the volume viscosity spectrum via [29]

$$\begin{aligned} \tilde{\zeta}(\vec{k} = 0, \omega) &= \int_0^\infty e^{-i\omega t} \zeta(t) dt, \\ &= \frac{V}{k_B T} \int_0^\infty e^{-i\omega t} \langle \delta P(t) \delta P(0) \rangle dt. \end{aligned} \quad (\text{M3})$$

For the Fourier transformation of the viscosity data, and the memory kernel data as well, we use the FFT algorithm implemented in numpy v. 1.18.5 [80], where we assume the input signal $x(t)$ to be single-sided, i.e. $x(t < 0) = 0$. All data in time domain are truncated at 10 ps.

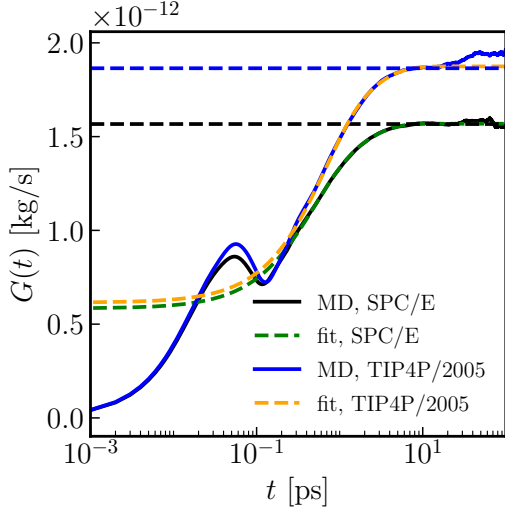


FIG. 11. Running integrals $G(t) = \int_0^t \Gamma(t') dt'$ of the memory kernels in fig. 1 together with fit functions according to Eq. L1. The horizontal dashed lines denote values of the friction coefficient $\gamma_0 = \sum_{j=I}^V \gamma_{0,j}$ obtained from the fits in the main text (tab. I).

Appendix N: Low- and High-Frequency Scaling of the Friction Function of a Sphere

For the real part of the friction in Eq. 8, we analytically obtain the asymptotic behavior, with shear viscosity and volume viscosity given by the models in Eqs. 18 and 21

$$\frac{\text{Re } \tilde{\Gamma}^{hyd}(\omega)}{6\pi\eta_0 a} \simeq \begin{cases} \omega \rightarrow 0 & \frac{1+2\hat{b}}{1+3\hat{b}} + \frac{a(1+2\hat{b})^2 \sqrt{\omega\rho_0/\eta_0}}{\sqrt{2}(1+3\hat{b})^2} \\ & + \mathcal{O}(\omega^{-2}), \\ \omega \rightarrow \infty & \\ \text{if } \tilde{\zeta} = \zeta_0 & \frac{2a}{9} \Phi_- \frac{(\alpha_\infty^+)^2}{2\lambda_\infty^+} \omega^{1/2}, \\ \text{otherwise} & \frac{2a}{9} (\Phi_+ \frac{(\alpha_\infty^+)^2}{\lambda_\infty^+} - \Phi_- C_\infty) \omega^{-3}, \end{cases} \quad (\text{N1})$$

with the constants

$$\Phi_+ = \left(\sum_{i=I}^{VI} \frac{\eta_{0,j}}{\tau_{o,j}^4} \right) / \eta_0, \quad (\text{N2})$$

$$\Phi_- = \left(\sum_{i=I}^{VI} \frac{\eta_{0,j} \tau_{n,j}}{\tau_{o,j}^2} \right) / \eta_0, \quad (\text{N3})$$

$$\eta_0 = \sum_{j=I}^{VII} \eta_{0,j}. \quad (\text{N4})$$

The constant C_∞ is given by:

$$C_\infty = \frac{2\alpha_\infty^+ \alpha_\infty^- \lambda_\infty^+ - (\alpha_\infty^+)^2 \lambda_\infty^-}{(\lambda_\infty^+)^2}. \quad (\text{N5})$$

Here, we introduced high-frequency convergence values for the inverse length scales α_∞^+ , λ_∞^+ , α_∞^- , λ_∞^- and λ_c .

They are determined by

$$\alpha_\infty^- = \frac{1}{2} \frac{\sqrt{\rho_0 \tilde{\eta}_\infty^-}}{\tilde{\eta}_\infty^+}, \quad \lambda_\infty^- = \frac{1}{2} \frac{\sqrt{\rho_0 \tilde{Z}_\infty^-}}{\tilde{Z}_\infty^+}, \quad (\text{N6})$$

$$\alpha_\infty^+ = \sqrt{\frac{\rho_0}{\tilde{\eta}_\infty^-}}, \quad \lambda_\infty^+ = \sqrt{\frac{\rho_0}{\tilde{Z}_\infty^-}}, \quad \lambda_c = \sqrt{\rho_0 / 2 \sum_{i=I}^{VII} \zeta_{0,j}},$$

where $\tilde{\eta}_\infty^+$, $\tilde{\eta}_\infty^-$, \tilde{Z}_∞^+ and \tilde{Z}_∞^- are comprised by the steady-state viscosities and relaxations times in the used models for the shear and volume viscosities in Eqs. 18 and 21, with $\tilde{Z}(\omega) = 4\tilde{\eta}(\omega)/3 + \tilde{\zeta}(\omega) - i\rho_0 c^2/\omega$

$$\tilde{\eta}_\infty^+ = \frac{\left(\sum_{i=I}^{VI} \frac{\eta_{0,j} \tau_{n,j}}{\tau_{o,j}^2} \right)^2}{\sum_{i=I}^{VI} \frac{\eta_{0,j}}{\tau_{o,j}^4}}, \quad (\text{N7})$$

$$\tilde{\eta}_\infty^- = \left(\sum_{i=I}^{VI} \frac{\eta_{0,j} \tau_{n,j}}{\tau_{o,j}^2} \right), \quad (\text{N8})$$

$$\tilde{Z}_\infty^+ = \frac{\left(\sum_{i=I}^{VI} \frac{4\eta_{0,j} \tau_{n,j}}{3\tau_{o,j}^2} + \sum_{i=I}^V \frac{\zeta_{0,j} \tau_{v,j}}{\tau_{w,j}^2} - \rho_0 c^2 \right)^2}{\sum_{i=I}^{VI} \frac{4\eta_{0,j}}{3\tau_{o,j}^4} + \sum_{i=I}^V \frac{\zeta_{0,j}}{\tau_{w,j}^4}}, \quad (\text{N9})$$

$$\tilde{Z}_\infty^- = \sum_{i=I}^{VI} \frac{4\eta_{0,j} \tau_{n,j}}{3\tau_{o,j}^2} + \sum_{i=I}^V \frac{\zeta_{0,j} \tau_{v,j}}{\tau_{w,j}^2} - \rho_0 c^2. \quad (\text{N10})$$

For $\tilde{\zeta}(\omega) \neq \zeta_0$, the real part of the friction $\tilde{\Gamma}^{hyd}(\omega)$ in Eq. 8 scales with $\sim \omega^{-3}$ for high frequencies. This stems from our choice of exponential-oscillatory models for shear and volume viscosity, where the real part of the components scales with ω^{-4} and imaginary part scales with ω^{-1} .

For completeness, the imaginary part of the friction function has the following asymptotic scaling

$$\frac{\text{Im } \tilde{\Gamma}^{hyd}(\omega)}{6\pi\eta_0 a} \simeq \begin{cases} \omega \rightarrow 0 & \frac{a(1+2\hat{b})^2 \sqrt{\omega\rho_0/\eta_0}}{\sqrt{2}(1+3\hat{b})^2} \\ & + \mathcal{O}(\omega), \\ \omega \rightarrow \infty & \\ \text{if } \tilde{\zeta} = \zeta_0 & \frac{2}{9} \Phi_- \frac{(\alpha_\infty^+)^2 a}{2\lambda_\infty^+} \omega^{1/2}, \\ \text{otherwise} & \frac{2}{9} \Phi_- \frac{(\alpha_\infty^+)^2 a}{\lambda_\infty^+} \omega^0 + \mathcal{O}\left(\frac{1}{\hat{b}} \omega^{-2}\right). \end{cases} \quad (\text{N11})$$

Thus, we see that at high frequencies for vanishing volume viscosity, i.e. $\tilde{\zeta}(\omega) \rightarrow 0$ as $\omega \rightarrow \infty$, the imaginary part of the friction converges to a constant value depending on the steady-state viscosity constants and time scales.

The friction in the frequency domain differs only marginally for frequency-dependent volume viscosity and for vanishing volume viscosity, i.e. $\tilde{\zeta} = 0$. For $\tilde{\zeta} = 0$, the

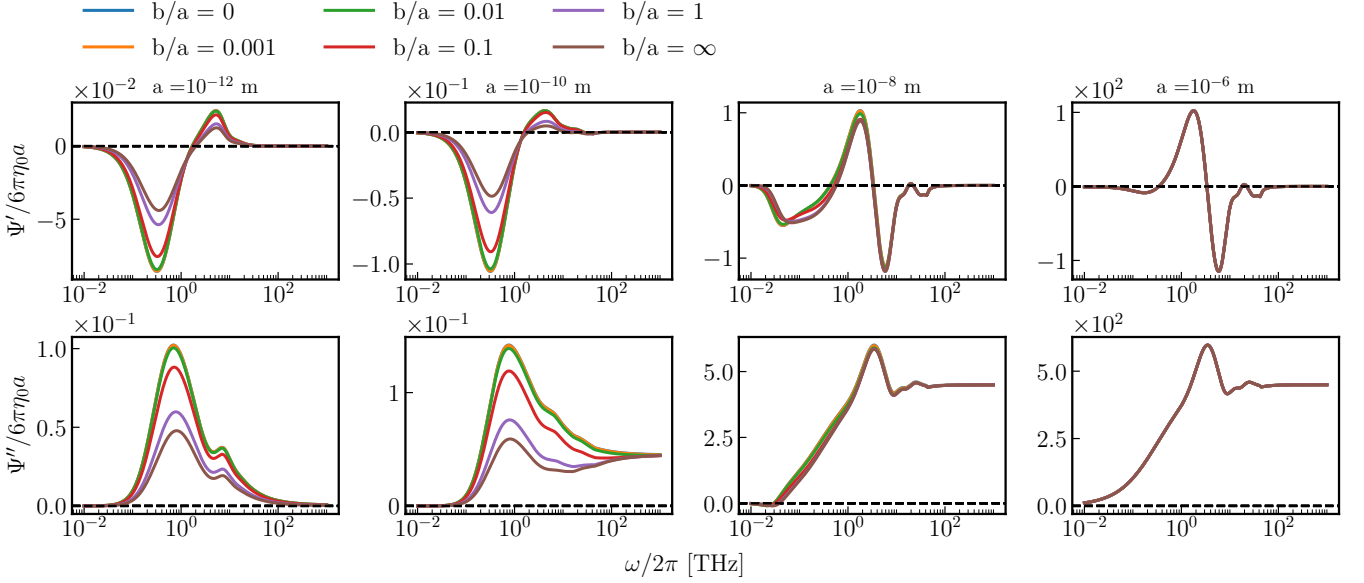


FIG. 12. Differences of the real and imaginary parts between the friction functions of a sphere given by Eq. 8 with the fitted model of the frequency-dependent volume viscosity in fig. 3 (solid lines in fig. 4) and with vanishing volume viscosity ($\zeta = 0$, dotted lines in fig. 4), denoted as Ψ' and Ψ'' (see Eqs. N12 and N13), for various slip lengths b and sphere radii a .

friction has the same asymptotic behavior as for $\tilde{\zeta}(\omega)$ in Eq. N1, with modified constants. In fig. 12 we show the difference between the friction functions, given by Eq. 8, with the fitted model of the frequency-dependent result in fig. 3 (solid lines in fig. 4) and with vanishing volume viscosity ($\zeta = 0$, dotted lines in fig. 4)

$$\Psi' = \text{Re } \tilde{\Gamma}^{hyd} - \text{Re } \tilde{\Gamma}^{hyd}(\tilde{\zeta} = 0), \quad (\text{N12})$$

$$\Psi'' = \text{Im } \tilde{\Gamma}^{hyd} - \text{Im } \tilde{\Gamma}^{hyd}(\tilde{\zeta} = 0). \quad (\text{N13})$$

We see distinct features in the difference spectrum. However, the absolute values of the differences are small compared to the absolute friction functions in fig. 4.

Appendix O: Comparison of the Friction with the Generalized Stokes-Einstein Relation

In fig. 13, we investigate the influence of the decay constants α^{-1} and λ^{-1} , where we show the difference spectrum between the full friction in Eq. 8 and the friction in the limit $\alpha \rightarrow 0$ and $\lambda \rightarrow 0$

$$\Omega' = \text{Re } \tilde{\Gamma}^{hyd} - \text{Re } \tilde{\Gamma}^{hyd}(\alpha \rightarrow 0, \lambda \rightarrow 0), \quad (\text{O1})$$

$$\Omega'' = \text{Im } \tilde{\Gamma}^{hyd} - \text{Im } \tilde{\Gamma}^{hyd}(\alpha \rightarrow 0, \lambda \rightarrow 0). \quad (\text{O2})$$

In this limit the friction of the sphere goes to

$$\tilde{\Gamma}^{hyd}(\omega) = 6\pi\tilde{\eta}(\omega)a \frac{1 + 2\hat{b}}{1 + 3\hat{b}}, \quad (\text{O3})$$

which is the generalized Stokes-Einstein relation (GSER) with slip. In fig. 13, we observe a significant dependence of the difference on the radius, where a higher radius leads to a higher difference between the full friction

function and the GSER result. For radii in the range of single water molecules, i.e. $a \approx 10^{-10}$ m, the maximum in the difference spectrum of the real parts lies at the pronounced oscillation with resonance frequency $f_{r,III} \approx 7.11$ THz (vertical dashed line) with differences between 5 and 11 % of the static friction without slip, depending on the slip coefficient. This shows that, for frequencies in the THz regime, the decay constants α^{-1} and λ^{-1} have a non-negligible effect on the friction of the sphere.

Appendix P: Origin of the Memory Kernel with Exponential High-Frequency Scaling

An exponential decrease of the Fourier-transformed memory kernel for high frequencies originates in the short-time properties of the velocity autocorrelation function (VACF). Following [43], we assume that the VACF has the form

$$C^{vv}(t) = \langle v^2 \rangle [1 + (t/\tau)^2]^{-1}, \quad (\text{P1})$$

with $\langle v^2 \rangle = k_B T/m$ and $\tau > 0$. The VACF fulfills the requirement of time-reversibility, i.e. $C^{vv}(t) = C^{vv}(-t)$, and only even powers contribute in the short-time expansion, i.e. $C^{vv}(t) \approx \langle v^2 \rangle [1 - t^2/\tau^2 + \mathcal{O}(t^4)]$. From the GLE in Eq. 12, we can derive a relation between the single-sided velocity autocorrelation function, $C_+^{vv}(t) = \Theta(t)C^{vv}(t)$, and the single-sided memory kernel $\Gamma_+(t)$ in Fourier space

$$\tilde{C}_+^{vv}(\omega) = \frac{i\omega k_B T}{i\omega \tilde{\Gamma}_+(\omega) - m\omega^2}. \quad (\text{P2})$$

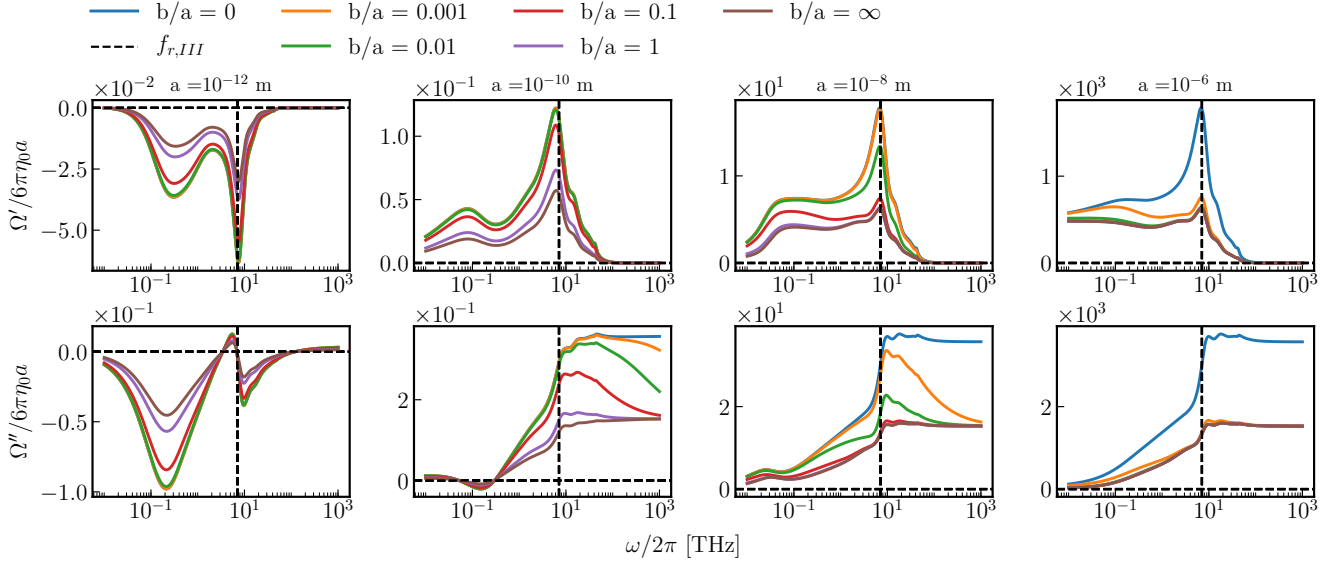


FIG. 13. Differences of the real and imaginary parts between the friction functions of a sphere given by Eq. 8 with the fitted models of the frequency-dependent shear and volume viscosity (solid lines in fig. 4) and in the limit $\alpha \rightarrow 0$ and $\lambda \rightarrow 0$ (Eq. O3, generalized Stokes-Einstein relation), denoted as Ω' and Ω'' (see Eqs. O1 and O2), for various slip lengths b and sphere radii a . The vertical dashed lines denote the pronounced oscillation with resonance frequency $f_{r,III} \approx 7.11$ THz (Eq. 19).

We show the derivation of this expression in Appendix T. The VACF in Eq. P1 can be rewritten as

$$C^{vv}(t) = \frac{\langle v^2 \rangle}{1 + (t/\tau)^2}, \quad (\text{P3})$$

$$= \frac{\langle v^2 \rangle \tau^2}{\tau^2 + t^2}, \quad (\text{P4})$$

$$= \frac{\langle v^2 \rangle \tau^2}{(\tau - it)(\tau + it)}, \quad (\text{P5})$$

$$= \langle v^2 \rangle \tau^2 \frac{2\tau + it - it}{2\tau(\tau - it)(\tau + it)}, \quad (\text{P6})$$

$$= \langle v^2 \rangle \tau^2 \left(\frac{1}{2\tau(\tau - it)} + \frac{1}{2\tau(\tau + it)} \right), \quad (\text{P7})$$

$$= \frac{\langle v^2 \rangle \tau}{2} \left(\frac{1}{\tau - it} + \frac{1}{\tau + it} \right). \quad (\text{P8})$$

With this, the single-sided Fourier transformation of $C^{vv}(t)$ can be written as

$$\tilde{C}_+^{vv}(\omega) = \langle v^2 \rangle \int_{-\infty}^{\infty} dt \theta(t) e^{-i\omega t} C^{vv}(t), \quad (\text{P9})$$

$$= \frac{\langle v^2 \rangle \tau}{2} \int_0^{\infty} dt e^{-i\omega t} \left(\frac{1}{\tau - it} + \frac{1}{\tau + it} \right), \quad (\text{P10})$$

from which the symmetric VACF follows as [43]

$$C^{vv}(t) = \frac{1}{\pi} \int_{-\infty}^{\infty} d\omega e^{i\omega t} \text{Re} \tilde{C}_+^{vv}(\omega). \quad (\text{P11})$$

Using Eq. P11 the real part of $\tilde{C}_+^{vv}(\omega)$ is $\text{Re} \tilde{C}_+^{vv}(\omega) = (\langle v^2 \rangle / 2) \tau \pi e^{-|\omega\tau|}$

$$C^{vv}(t) = \frac{\langle v^2 \rangle \tau}{2} \int_{-\infty}^{\infty} d\omega e^{i\omega t} e^{-|\omega\tau|}, \quad (\text{P12})$$

$$= \frac{\langle v^2 \rangle \tau}{2} \left(\int_0^{\infty} d\omega e^{-\omega(\tau - it)} + \int_{-\infty}^0 d\omega e^{\omega(\tau + it)} \right), \quad (\text{P13})$$

$$= \frac{\langle v^2 \rangle \tau}{2} \left(\frac{1}{\tau - it} + \frac{1}{\tau + it} \right). \quad (\text{P14})$$

Since the single-sided VACF is zero for $t < 0$, the imaginary part of $\tilde{C}_+^{vv}(\omega)$ is related to the real part via the Kramers-Kronig relation [81, 82]

$$\text{Im} \tilde{C}_+^{vv}(\omega) = -\frac{1}{\pi} \mathcal{P} \int_{-\infty}^{\infty} d\omega' \frac{\text{Re} \tilde{C}_+^{vv}(\omega')}{\omega' - \omega}, \quad (\text{P15})$$

where \mathcal{P} is the principle part of the integral

$$\mathcal{P} = \lim_{\epsilon \rightarrow 0} \left(\frac{1}{\omega - \omega' + i\epsilon} + \frac{1}{\omega - \omega' - i\epsilon} \right). \quad (\text{P16})$$

Thus, the imaginary part reads

$$\text{Im} \tilde{C}_+^{vv}(\omega) = -\frac{\langle v^2 \rangle \tau}{2} \mathcal{P} \int_{-\infty}^{\infty} d\omega' \frac{e^{-|\omega'\tau|}}{\omega' - \omega}, \quad (\text{P17})$$

$$= \frac{\langle v^2 \rangle \tau}{2} \mathcal{P} \left(\int_{-\infty}^0 d\omega' \frac{e^{\omega'\tau}}{-\omega' - \omega} + \int_0^{\infty} d\omega' \frac{e^{-\omega'\tau}}{\omega' - \omega} \right), \quad (\text{P18})$$

$$= \frac{\langle v^2 \rangle \tau}{2} \left(\int_{-\infty}^{\omega\tau} e^{-\omega\tau} \frac{e^u}{u} du - \int_{-\infty}^{-\omega\tau} e^{\omega\tau} \frac{e^u}{u} du \right), \quad (\text{P19})$$

$$= \frac{\langle v^2 \rangle \tau}{2} [e^{-\omega\tau} \text{Ei}(\omega\tau) - e^{\omega\tau} \text{Ei}(-\omega\tau)], \quad (\text{P20})$$

where $Ei(\cdot)$ is the exponential integral. The result for the Fourier transformation of the single-sided VACF is

$$\tilde{C}_+^{vv}(\omega) = D e^{-|\omega\tau|} + i \frac{D_0}{\pi} [e^{-\omega\tau} Ei(\omega\tau) - e^{\omega\tau} Ei(-\omega\tau)], \quad (\text{P21})$$

where $D_0 = \langle v^2 \rangle \tau \pi / 2$. Using Eq. P2, we obtain an expression for the single-sided memory kernel

$$\tilde{\Gamma}_+(\omega) = \frac{k_B T}{\tilde{C}_+^{vv}(\omega)} - im\omega. \quad (\text{P22})$$

The real part of the memory kernel is obtained by

$$\text{Re } \tilde{\Gamma}_+(\omega) = k_B T \frac{\text{Re } \tilde{C}_+^{vv}(\omega)}{[\text{Re } \tilde{C}_+^{vv}(\omega)]^2 + [\text{Im } \tilde{C}_+^{vv}(\omega)]^2}. \quad (\text{P23})$$

For high frequencies, the real part of $\tilde{C}_+^{vv}(\omega)$ in Eq. P10 scales with $D_0 e^{-|\omega\tau|}$ and the imaginary part scales with $\langle v^2 \rangle \omega^{-1}$, which we obtain by numerical evaluation of the exponential integral in Eq. P21. For high frequencies, the imaginary part dominates in the denominator in Eq. P23, and the real part of the memory kernel scales exponentially with

$$\lim_{\omega \rightarrow \infty} \text{Re } \tilde{\Gamma}_+(\omega) \approx \frac{k_B T}{D_0} \left(\frac{\tau \pi}{2} \right)^2 \omega^2 e^{-|\omega\tau|}. \quad (\text{P24})$$

Appendix Q: Short-Time Expansion of the Exponential-Oscillatory Memory Kernel

The memory kernel in Eq. F6 is not analytic because of the Heaviside function prefactor $\Theta(t)$. $\Gamma(|t|)$ can be expanded for short times $t \rightarrow 0$

$$\begin{aligned} \lim_{t \rightarrow 0} \Gamma(|t|) &\approx \frac{\gamma_0 \tau_n}{\tau_o^2} - \frac{\gamma_0}{8 \tau_n \tau_o^2} (\kappa^2 + 1) t^2 \\ &+ \frac{\gamma_0}{24 \tau_n^2 \tau_o^2} (\kappa^2 + 1) |t|^3 \\ &+ \frac{\gamma_0}{192 \tau_n^3 \tau_o^2} \left(\frac{\kappa^4}{2} - \kappa^2 - \frac{3}{2} \right) t^4 \\ &+ \mathcal{O}(|t|^5). \end{aligned} \quad (\text{Q1})$$

We see that the third derivative is discontinuous at $t = 0$. Hence the memory kernel is not analytic.

Appendix R: Velocity Autocorrelation Function from the Exponential-Oscillatory Memory Kernel

Using the identity

$$\tilde{C}^{vv}(\omega) = -2k_B T \omega \text{Im } \tilde{\chi}(\omega), \quad (\text{R1})$$

which we derive in Appendix T, and the exponential-oscillatory memory kernel in Eq. F6, we can obtain an analytical expression for the velocity-correlation function

in frequency space. An inverse Fourier transformation for the VACF is generally difficult. Hence, we investigate the behavior of the VACF for the exponential-oscillatory memory kernel for short times

$$C^{vv}(t) = \sum_{j=0}^{\infty} \frac{t^j}{j!} \frac{d^j C^{vv}(s)}{ds^j} \Big|_{s=0}. \quad (\text{R2})$$

Using our definition of the inverse Fourier transformation, we have

$$\frac{d^j C^{vv}(t)}{dt^j} \Big|_{t=0} = \int_{-\infty}^{\infty} \frac{d\omega}{2\pi} (i\omega)^j \tilde{C}^{vv}(\omega). \quad (\text{R3})$$

Using this identity, we can investigate the convergence of the short-time expansion terms of $C^{vv}(t)$ for a given memory kernel $\tilde{\Gamma}_+(\omega)$. We first check the procedure using the memory kernel with exponential high-frequency scaling (Appendix P). Using $\tilde{C}_+^{vv}(\omega)$ in Eq. P21 and the identity $\tilde{C}^{vv}(\omega) = 2 \text{Re } \tilde{C}_+^{vv}(\omega)$ (Appendix T), the short-time expansion of $C^{vv}(t)$ in real space is

$$C^{vv}(t) \approx \frac{k_B T}{m} \left[1 - \frac{t^2}{\tau^2} + \mathcal{O}(t^4) \right], \quad (\text{R4})$$

in agreement with the short-time expansion of $C^{vv}(t)$ in Appendix P.

Inserting the exponential-oscillatory memory kernel in Eq. F6 into Eq. R3, we find that the sixth term diverges and only the zeroth, second and fourth expansion term converge in real space, i.e. $C^{vv}(t) \approx \frac{k_B T}{m} (1 - At^2 + Bt^4)$, where A and B are determined from Eq. R3. This follows from the fact that for high frequencies $\tilde{C}^{vv}(\omega)$ scales with $\sim \frac{2k_B T \gamma_0}{\tau_o^3 m} \omega^{-6}$, which we obtain by inserting the expression in Eq. F6 into Eq. R1. Thus, we conclude that the exponential-oscillatory memory kernel correspond to a non-analytic velocity autocorrelation function in time domain.

Appendix S: Origin of the Memory Kernel with Gaussian High-Frequency Scaling

We assume that the VACF has the form of a Gaussian function

$$C^{vv}(t) = \langle v^2 \rangle e^{-t^2/\tau^2}, \quad (\text{S1})$$

which is symmetric in time, i.e. $C^{vv}(t) = C^{vv}(-t)$, and only even powers contribute in the short-time expansion, i.e. $C^{vv}(t) \approx \langle v^2 \rangle [1 - t^2/\tau^2 + \mathcal{O}(t^4)]$. We obtain the Fourier-transformed single-sided VACF similar as in Appendix P. We find that the real part of $\tilde{C}_+^{vv}(\omega)$ is $\text{Re } \tilde{C}_+^{vv}(\omega) = \langle v^2 \rangle \tau \sqrt{\pi} / 2 e^{-\omega^2 \tau^2 / 4}$, which we can check

by inserting this expression into Eq. P11

$$C^{vv}(t) = \frac{\langle v^2 \rangle \tau}{2\sqrt{\pi}} \int_{-\infty}^{\infty} d\omega e^{i\omega t} e^{-\omega^2 \tau^2 / 4}, \quad (\text{S2})$$

$$= \frac{\langle v^2 \rangle \tau}{2\sqrt{\pi}} \int_{-\infty}^{\infty} d\omega e^{-t^2 / \tau^2} e^{-\frac{1}{\tau^2} (\frac{\omega \tau^2}{2} - it)^2}, \quad (\text{S3})$$

$$= \frac{\langle v^2 \rangle \tau}{2\sqrt{\pi}} e^{-t^2 / \tau^2} \int_{-\infty}^{\infty} d\omega e^{-\omega^2 \tau^2 / 4}, \quad (\text{S4})$$

$$= \frac{\langle v^2 \rangle \tau}{2\sqrt{\pi}} e^{-t^2 / \tau^2} \frac{2\sqrt{\pi}}{\tau}, \quad (\text{S5})$$

$$= \langle v^2 \rangle e^{-t^2 / \tau^2}. \quad (\text{S6})$$

The imaginary part of $\tilde{C}_+^{vv}(\omega)$ can be determined by the Kramers-Kronig relation in Eq. P15

$$\text{Im } \tilde{C}_+^{vv}(\omega) = -\frac{\langle v^2 \rangle \tau}{2\sqrt{\pi}} \mathcal{P} \int_{-\infty}^{\infty} d\omega' \frac{e^{-\omega'^2 \tau^2 / 4}}{\omega' - \omega}, \quad (\text{S7})$$

$$= -\frac{\langle v^2 \rangle \tau}{2\sqrt{\pi}} \mathcal{I}(\omega), \quad (\text{S8})$$

which defines the function $\mathcal{I}(\omega)$. The complex function $\tilde{C}_+^{vv}(\omega)$ thus follows as

$$\tilde{C}_+^{vv}(\omega) = D_0 e^{-\omega^2 \tau^2 / 4} + i D_0 \mathcal{I}(\omega), \quad (\text{S9})$$

where $D_0 = \langle v^2 \rangle \tau \sqrt{\pi} / 2$. Using Eq. P2, we obtain an expression for the single-sided memory kernel. For high frequencies, the real part of $\tilde{C}_+^{vv}(\omega)$ scales with $D_0 e^{-\omega^2 \tau^2 / 4}$ and the imaginary part scales with $\langle v^2 \rangle \omega^{-1}$, which we obtain by numerical evaluation of the imaginary part in Eq. S9. The real part of the memory kernel in Eq. P23 scales like a Gaussian function with

$$\lim_{\omega \rightarrow \infty} \text{Re } \tilde{\Gamma}_+(\omega) \approx \frac{k_B T}{D_0} \left(\frac{\tau \sqrt{\pi}}{2} \right)^2 \omega^2 e^{-\omega^2 \tau^2 / 4}. \quad (\text{S10})$$

Appendix T: Derivation of Eq. P2

We start from the Fourier-transformed GLE in Eq. 14, i.e. $\tilde{v}(\omega) = i\omega \tilde{\chi}(\omega) \tilde{F}_R(\omega)$, where $\tilde{\chi}(\omega) = (i\omega \tilde{\Gamma}_+(\omega) - m\omega^2)^{-1}$. The fluctuation-dissipation theorem, i.e. $\langle F_R(t) F_R(t') \rangle = k_B T \Gamma(|t - t'|)$, in Fourier space reads

$$\langle \tilde{F}_R(\omega) \tilde{F}_R(\omega') \rangle = \quad (\text{T1})$$

$$k_B T \int_{-\infty}^{\infty} dt e^{-i\omega t} \int_{-\infty}^{\infty} dt' e^{-i\omega' t'} \Gamma(t - t'),$$

$$= k_B T \int_{-\infty}^{\infty} dt' e^{-i(\omega + \omega')t} \int_{-\infty}^{\infty} dt e^{-i\omega(t-t')} \Gamma(t - t'), \quad (\text{T2})$$

$$= k_B T \int_{-\infty}^{\infty} dt' e^{-i(\omega + \omega')t'} \tilde{\Gamma}(\omega), \quad (\text{T3})$$

$$= 2\pi k_B T \delta(\omega + \omega') \tilde{\Gamma}(\omega). \quad (\text{T4})$$

Using this identity, we obtain for the Fourier transformation of the VACF

$$\tilde{C}^{vv}(\omega) = \int_{-\infty}^{\infty} \frac{d\omega'}{2\pi} e^{-i\omega(t-t)} \langle \tilde{v}(\omega) \tilde{v}(\omega') \rangle, \quad (\text{T5})$$

$$= \int_{-\infty}^{\infty} \frac{d\omega'}{2\pi} \langle i\omega \tilde{x}(\omega) i\omega' \tilde{x}(\omega') \rangle, \quad (\text{T6})$$

$$= - \int_{-\infty}^{\infty} \frac{d\omega'}{2\pi} \langle \omega \tilde{\chi}(\omega) \tilde{F}_R(\omega) \omega' \tilde{\chi}(\omega') \tilde{F}_R(\omega') \rangle, \quad (\text{T7})$$

$$= -k_B T \int_{-\infty}^{\infty} d\omega' \omega \omega' \tilde{\chi}(\omega) \tilde{\chi}(\omega') \delta(\omega + \omega') \tilde{\Gamma}(\omega), \quad (\text{T8})$$

$$= k_B T \omega^2 \tilde{\chi}(\omega) \tilde{\chi}(-\omega) \tilde{\Gamma}(\omega), \quad (\text{T9})$$

$$= k_B T \omega^2 \tilde{\Gamma}(\omega) \frac{\tilde{\chi}(-\omega) - \tilde{\chi}(\omega)}{\frac{1}{\tilde{\chi}(\omega)} - \frac{1}{\tilde{\chi}(-\omega)}}, \quad (\text{T10})$$

$$= k_B T \omega^2 \tilde{\Gamma}(\omega) \frac{\tilde{\chi}(-\omega) - \tilde{\chi}(\omega)}{i\omega(\tilde{\Gamma}_+(\omega) + \tilde{\Gamma}_+(-\omega))}. \quad (\text{T11})$$

Since $\chi(t)$ is a real function, we have $\tilde{\chi}(-\omega) - \tilde{\chi}(\omega) = \tilde{\chi}^*(\omega) - \tilde{\chi}(\omega) = -2i \text{Im } \tilde{\chi}(\omega)$, where $\tilde{\chi}^*(\omega)$ is the complex conjugated function of $\tilde{\chi}(\omega)$. For any function $f(t)$ symmetric in t , as $\Gamma(t)$ and $C_{vv}(t)$, we have

$$\tilde{f}_+(\omega) + \tilde{f}_+(-\omega) = \tilde{f}_+(\omega) + \tilde{f}_+^*(\omega), \quad (\text{T12})$$

$$= \int_{-\infty}^{\infty} dt f_+(t) e^{-i\omega t} + \int_{-\infty}^{\infty} dt f_+(t) e^{i\omega t}, \quad (\text{T13})$$

$$= \int_{-\infty}^{\infty} dt f(t) \theta(t) e^{-i\omega t} + \int_{-\infty}^{\infty} dt f(t) \theta(-t) e^{-i\omega t}, \quad (\text{T14})$$

$$= \tilde{f}(\omega). \quad (\text{T15})$$

Inserting this identity for $\tilde{\Gamma}_+(\omega)$ into Eq. T11, we obtain

$$\tilde{C}^{vv}(\omega) = -2k_B T \omega \text{Im } \tilde{\chi}(\omega), \quad (\text{T16})$$

and

$$\text{Re } \tilde{C}_+^{vv}(\omega) = -k_B T \omega \text{Im } \tilde{\chi}(\omega), \quad (\text{T17})$$

$$= k_B T \omega \text{Re } (i\tilde{\chi}(\omega)), \quad (\text{T18})$$

where we use $\tilde{C}^{vv}(\omega) = \tilde{C}_+^{vv}(\omega) + (\tilde{C}_+^{vv}(\omega))^* = 2\text{Re } \tilde{C}_+^{vv}(\omega)$. For the single-sided VACF, we finally obtain

$$\begin{aligned} \tilde{C}_+^{vv}(\omega) &= i\omega k_B T \tilde{\chi}(\omega), \quad (\text{T19}) \\ &= \frac{i\omega k_B T}{i\omega \tilde{\Gamma}_+(\omega) - m\omega^2}. \end{aligned}$$

Here we use the fact, employing the Kramers-Kronig relations, that if the real parts of two analytic functions are equal (Eq. T18), the total complex functions are equal [8]. Note that the identity in Eq. T19 only holds if $\tilde{C}_+^{vv}(\omega)$ and $\tilde{\chi}(\omega)$ are analytic in the time domain.

-
- [1] H. Mori. Transport, Collective Motion, and Brownian Motion. *Progress of Theoretical Physics*, 33(3):423–455, 1965.
- [2] R. Zwanzig. Time-Correlation Functions and Transport Coefficients in Statistical Mechanics. *Annual Review of Physical Chemistry*, 16(1):67–102, 1965.
- [3] D. Lesnicki, R. Vuilleumier, A. Carof, and B. Rotenberg. Molecular Hydrodynamics from Memory Kernels. *Physical Review Letters*, 116(14):147804, 2016.
- [4] A. Carof, R. Vuilleumier, and B. Rotenberg. Two Algorithms to Compute Projected Correlation Functions in Molecular Dynamics Simulations. *The Journal of Chemical Physics*, 140(12):124103, 2014.
- [5] G. Jung, M. Hanke, and F. Schmid. Iterative Reconstruction of Memory Kernels. *Journal of Chemical Theory and Computation*, 13(6):2481–2488, 2017.
- [6] G. Jung and F. Schmid. Frequency-Dependent Hydrodynamic Interaction Between Two Solid Spheres. *Physics of Fluids*, 29(12):126101, 2017.
- [7] J. O. Daldrop, B. G. Kowalik, and R. R. Netz. External Potential Modifies Friction of Molecular Solutes in Water. *Physical Review X*, 7(4):041065, 2017.
- [8] B. Kowalik, J. O. Daldrop, J. Kappler, J. C. F. Schulz, A. Schlaich, and R. R. Netz. Memory-Kernel Extraction for Different Molecular Solutes in Solvents of Varying Viscosity in Confinement. *Physical Review E*, 100(1):012126, 2019.
- [9] B. G. Mitterwallner, C. Schreiber, J. O. Daldrop, J. O. Rädler, and R. R. Netz. Non-Markovian Data-Driven Modeling of Single-Cell Motility. *Physical Review E*, 101(3):032408, 2020.
- [10] J. O. Daldrop, J. Kappler, F. N. Brünig, and R. R. Netz. Butane Dihedral Angle Dynamics in Water is Dominated by Internal Friction. *Proceedings of the National Academy of Sciences*, 115(20):5169–5174, 2018.
- [11] C. Ayaz, F. N. Tepper, L. and Brünig, J. Kappler, J. O. Daldrop, and R. R. Netz. Non-Markovian Modeling of Protein Folding. *Proceedings of the National Academy of Sciences*, 118(31), 2021.
- [12] P. Sollich, F. Lequeux, P. Hébraud, and M. E. Cates. Rheology of Soft Glassy Materials. *Physical Review Letters*, 78(10):2020, 1997.
- [13] D. Mizuno, C. Tardin, C. F. Schmidt, and F. C. MacKintosh. Nonequilibrium Mechanics of Active Cytoskeletal Networks. *Science*, 315(5810):370–373, 2007.
- [14] D. Winter, J. Horbach, P. Virnau, and K. Binder. Active Nonlinear Microrheology in a Glass-Forming Yukawa Fluid. *Physical Review Letters*, 108(2):028303, 2012.
- [15] T. S. Chow and J. J. Hermans. Effect of Inertia on the Brownian Motion of Rigid Particles in a Viscous Fluid. *The Journal of Chemical Physics*, 56(6):3150–3154, 1972.
- [16] T. S. Chow and J. J. Hermans. Brownian Motion of a Spherical Particle in a Compressible Fluid. *Physica*, 65(1):156–162, 1973.
- [17] E. H. Hauge and A. Martin-Löf. Fluctuating Hydrodynamics and Brownian Motion. *Journal of Statistical Physics*, 7(3):259–281, 1973.
- [18] D. Bedeaux and P. Mazur. A Generalization of Faxén’s Theorem to Nonsteady Motion of a Sphere Through a Compressible Fluid in Arbitrary Flow. *Physica*, 78(3):505–515, 1974.
- [19] E. J. Hinch. Application of the Langevin Equation to Fluid Suspensions. *Journal of Fluid Mechanics*, 72(3):499–511, 1975.
- [20] P. Español. On the Propagation of Hydrodynamic Interactions.
- [21] B. U. Felderhof. Backtracking of a Sphere Slowing Down in a Viscous Compressible Fluid. *The Journal of Chemical Physics*, 123(4):044902, 2005.
- [22] D. Chakraborty. Velocity Autocorrelation Function of a Brownian Particle. *The European Physical Journal B*, 83(3):375–380, 2011.
- [23] R. Tatsumi and R. Yamamoto. Direct Numerical Simulation of Dispersed Particles in a Compressible Fluid. *Physical Review E*, 85(6):066704, 2012.
- [24] K. Mizuta, Y. Ishii, K. Kim, and N. Matubayasi. Bridging the Gap Between Molecular Dynamics and Hydrodynamics in Nanoscale Brownian Motions. *Soft Matter*, 15(21):4380–4390, 2019.
- [25] R. Zwanzig and M. Bixon. Hydrodynamic Theory of the Velocity Correlation Function. *Physical Review A*, 2(5):2005, 1970.
- [26] H. Metiu, D. W. Oxtoby, and K. F. Freed. Hydrodynamic Theory for Vibrational Relaxation in Liquids. *Physical Review A*, 15(1):361, 1977.
- [27] W. M. Slie, A. R. Donfor Jr, and T. A. Litovitz. Ultrasonic Shear and Longitudinal Measurements in Aqueous Glycerol. *The Journal of Chemical Physics*, 44(10):3712–3718, 1966.
- [28] M. Pelton, D. Chakraborty, E. Malachosky, P. Guyot-Sionnest, and J.E. Sader. Viscoelastic Flows in Simple Liquids Generated by Vibrating Nanostructures. *Physical Review Letters*, 111(24):244502, 2013.
- [29] J. S. Medina, R. Prosimiti, P. Villarreal, G. Delgado-Barrio, G. Winter, B. González, J. V. Alemán, and C. Collado. Molecular Dynamics Simulations of Rigid and Flexible Water Models: Temperature Dependence of Viscosity. *Chemical Physics*, 388(1-3):9–18, 2011.
- [30] G. S. Fanourgakis, J. S. Medina, and R. Prosimiti. Determining the Bulk Viscosity of Rigid Water Models. *The Journal of Physical Chemistry A*, 116(10):2564–2570, 2012.
- [31] J. C. F. Schulz, A. Schlaich, M. Heyden, R. R. Netz, and J. Kappler. Molecular Interpretation of the Non-Newtonian Viscoelastic Behavior of Liquid Water at High Frequencies. *Physical Review Fluids*, 5(10):103301, 2020.
- [32] A. Erbaş, R. Podgornik, and R. R. Netz. Viscous Compressible Hydrodynamics at Planes, Spheres and Cylinders with Finite Surface Slip. *The European Physical Journal E*, 32(2):147–164, 2010.
- [33] G. G. Stokes et al. On the Effect of the Internal Friction of Fluids on the Motion of Pendulums. 1851.
- [34] G. K. Batchelor. *An Introduction to Fluid Dynamics*. Cambridge university press, 2000.
- [35] S. Kim and S. J. Karrila. *Microhydrodynamics: Principles and Selected Applications*. Courier Corporation, 2013.
- [36] J.-P. Hansen and I. R. McDonald. *Theory of Simple Liquids*. Elsevier, 1990.
- [37] P. J. Davis and D.J. Evans. Comparison of Constant Pressure and Constant Volume Nonequilibrium Simulations of Sheared Model Decane. *The Journal of Chemical*

- Physics*, 100(1):541–547, 1994.
- [38] D. J. Evans and G. P. Morriss. *Statistical Mechanics of Nonequilibrium Liquids*. ANU Press, 2007.
- [39] L. D. Landau and E. M. Lifshits. *Fluid Mechanics*, volume 11. Pergamon Press Oxford, UK, 1959.
- [40] G. G. Stokes. On the Theories of the Internal Friction of Fluids in Motion, and of the Equilibrium and Motion of Elastic Solids. *Transactions of the Cambridge Philosophical Society*, 8, 1880.
- [41] F. Jaeger, O. K. Matar, and E. A. Müller. Bulk Viscosity of Molecular Fluids. *The Journal of Chemical Physics*, 148(17):174504, 2018.
- [42] K. R. Harris and L. A. Woolf. Temperature and Volume Dependence of the Viscosity of Water and Heavy Water at Low Temperatures. *Journal of Chemical & Engineering Data*, 49(4):1064–1069, 2004.
- [43] A. V. Straube, B. G. Kowalik, R. R. Netz, and Felix Höfling. Rapid Onset of Molecular Friction in Liquids Bridging Between the Atomistic and Hydrodynamic Pictures. *Communications Physics*, 3(1):1–11, 2020.
- [44] J. Kappler, J. O. Daldrop, F. N. Brünig, M. D. Boehle, and R. R. Netz. Memory-Induced Acceleration and Slowdown of Barrier Crossing. *The Journal of Chemical Physics*, 148(1):014903, 2018.
- [45] V. Klippenstein, M. Tripathy, G. Jung, F. Schmid, and N. F. A. van der Vegt. Introducing Memory in Coarse-Grained Molecular Simulations. *The Journal of Physical Chemistry B*, 2021.
- [46] D. Rozmanov and P.G. Kusalik. Transport Coefficients of the TIP4P-2005 Water Model. *The Journal of Chemical Physics*, 136(4):044507, 2012.
- [47] R. Mills. Self-Diffusion in Normal and Heavy Water in the Range 1-45. deg. *The Journal of Physical Chemistry*, 77(5):685–688, 1973.
- [48] K. T. Gillen, D. C. Douglass, and M. J. R. Hoch. Self-Diffusion in Liquid Water to -31 C. *The Journal of Chemical Physics*, 57(12):5117–5119, 1972.
- [49] F. Sedlmeier, S. Shadkhoo, R. Bruinsma, and R. R. Netz. Charge/Mass Dynamic Structure Factors of Water and Applications to Dielectric Friction and Electroacoustic Conversion. *The Journal of Chemical Physics*, 140(5):054512, 2014.
- [50] E. M. Lifshitz and L. D. Landau. *Course of Theoretical Physics: Fluid Mechanics*, 1987.
- [51] D. J. Acheson. *Elementary Fluid Dynamics*. Acoustical Society of America, 1991.
- [52] I. P. Omelyan, I. M. Mryglod, and M. V. Tokarchuk. Wavevector- and Frequency-Dependent Shear Viscosity of Water: the Modified Collective Mode Approach and Molecular Dynamics Calculations. *Condensed Matter Physics*, 2005.
- [53] N. M. Lacevic and J. E. Sader. Viscoelasticity of Glycerol at Ultra-High Frequencies Investigated via Molecular Dynamics Simulations. *The Journal of Chemical Physics*, 144(5):054502, 2016.
- [54] T. J. O’Sullivan, S. K. Kannam, D. Chakraborty, B. D. Todd, and J. E. Sader. Viscoelasticity of Liquid Water Investigated using Molecular Dynamics Simulations. *Physical Review Fluids*.
- [55] L. Bocquet and E. Charlaix. Nanofluidics, from Bulk to Interfaces. *Chemical Society Reviews*, 39(3):1073–1095, 2010.
- [56] P.V. Ruijgrok, P. Zijlstra, A.L. Tchegotareva, and M. Orrit. Damping of Acoustic Vibrations of Single Gold Nanoparticles Optically Trapped in Water. *Nano Letters*, 12(2):1063–1069, 2012.
- [57] A. Cunsolo, G. Ruocco, F. Sette, C. Masciovecchio, A. Mermet, G. Monaco, M. Sampoli, and R. Verbeni. Experimental Determination of the Structural Relaxation in Liquid Water. *Physical Review Letters*, 82(4):775, 1999.
- [58] D. M. Carey and G. M. Korenowski. Measurement of the Raman Spectrum of Liquid Water. *The Journal of Chemical Physics*, 108(7):2669–2675, 1998.
- [59] S. Carlson, F. N. Brünig, P. Loche, D. J. Bonthuis, and R. R. Netz. Exploring the Absorption Spectrum of Simulated Water from MHz to Infrared. *The Journal of Physical Chemistry A*, 124(27):5599–5605, 2020.
- [60] R. Schulz, Y. von Hansen, J. O. Daldrop, J. Kappler, F. Noé, and R. R. Netz. Collective Hydrogen-Bond Rearrangement Dynamics in Liquid Water. *The Journal of Chemical Physics*, 149(24):244504, 2018.
- [61] S. Tazi, A. Boğan, M. Salanne, V. Marry, P. Turq, and B. Rotenberg. Diffusion Coefficient and Shear Viscosity of Rigid Water Models. *Journal of Physics: Condensed Matter*, 24(28):284117, 2012.
- [62] M. A. González and J. L. F. Abascal. A Flexible Model for Water Based on TIP4P/2005. *The Journal of Chemical Physics*, 135(22):224516, 2011.
- [63] S. Zendeheroud, J. O. Daldrop, Y. von Hansen, and R. R. Netz. Generalized Molecular Stokes-Einstein and Stokes-Einstein-Debye Relations Including Finite Slip. *Unpublished*, 2022.
- [64] S. Pronk, S. Páll, R. Schulz, P. Larsson, P. Bjelkmar, R. Apostolov, M. R. Shirts, J. C. Smith, P. M. Kasson, D. van der Spoel, et al. GROMACS 4.5: a High-Throughput and Highly Parallel Open Source Molecular Simulation Toolkit. *Bioinformatics*, 29(7):845–854, 2013.
- [65] H. J. C. Berendsen and T. P. Grigera, J. R. and Straatsma. The Missing Term in Effective Pair Potentials. *Journal of Physical Chemistry*, 91(24):6269–6271, 1987.
- [66] J. L. F. Abascal and C. Vega. A General Purpose Model for the Condensed Phases of Water: TIP4P/2005. *The Journal of Chemical Physics*, 123(23):234505, dec 2005.
- [67] H. J. C. Berendsen, J. P. M. Postma, W. F. van Gunsteren, A. DiNola, and J. R. Haak. Molecular Dynamics with Coupling to an External Bath. *The Journal of Chemical Physics*, 81(8):3684–3690, 1984.
- [68] G. Bussi, D. Donadio, and M. Parrinello. Canonical Sampling Through Velocity Rescaling. *The Journal of Chemical Physics*, 126(1):014101, 2007.
- [69] T. Darden, D. York, and L. Pedersen. Particle Mesh Ewald: An $N \log(N)$ Method for Ewald Sums in Large Systems. *The Journal of Chemical Physics*, 98(12):10089–10092, jun 1993.
- [70] O. F. Lange and H. Grubmüller. Collective Langevin Dynamics of Conformational Motions in Proteins. *The Journal of Chemical Physics*, 124(21):214903, 2006.
- [71] V. Klippenstein and N. F. A. van der Vegt. Cross-Correlation Corrected Friction in (Generalized) Langevin Models. *The Journal of Chemical Physics*, 154(19):191102, 2021.
- [72] H. Vroylandt, L. Goudenège, P. Monmarché, F. Pietrucci, and B. Rotenberg. Likelihood-Based Parametric Estimator for Memory Kernel in Molecular Dynamics. *arXiv preprint arXiv:2110.04246*, 2021.
- [73] B. J. Berne and G. D. Harp. On the Calculation of Time Correlation Functions. *Adv. Chem. Phys.*, 17:63–

- 227, 1970.
- [74] J. E. Straub, M. Borkovec, and B. J. Berne. Calculation of Dynamic Friction on Intramolecular Degrees of Freedom. *Journal of Physical Chemistry*, 91(19):4995–4998, 1987.
- [75] R. Zwanzig. *Nonequilibrium Statistical Mechanics*. Oxford University Press, 2001.
- [76] M. Ceriotti, G. Bussi, and M. Parrinello. Colored-Noise Thermostats à la Carte. *Journal of Chemical Theory and Computation*, 6(4):1170–1180, 2010.
- [77] Z. Li, H. S. Lee, E. Darve, and G. E. Karniadakis. Computing the Non-Markovian Coarse-Grained Interactions Derived from the Mori-Zwanzig Formalism in Molecular Systems: Application to Polymer Melts. *The Journal of Chemical Physics*, 146(1):014104, 2017.
- [78] F. N. Brüning, O. Geburtig, A. von Canal, J. Kappler, and R. R. Netz. Time-Dependent Friction Effects on Vibrational Infrared Frequencies and Line Shapes of Liquid Water. *arXiv preprint arXiv:2201.01655*, 2022.
- [79] P. Virtanen, R. Gommers, T.E. Oliphant, Travis E., M. Haberland, T. Reddy, D. Cournapeau, E. Burovski, P. Peterson, W. Weckesser, J. Bright, S. J. van der Walt, J. Brett, M. and Wilson, K. J. Millman, N. Mayorov, A. R. J. Nelson, E. Jones, R. Kern, E. Larson, C. J. Carey, Í. Polat, Y. Feng, E. W. Moore, J. VanderPlas, D. Laxalde, J. Perktold, R. Cimrman, I. Henriksen, E. A. Quintero, C. R. Harris, A. M. Archibald, A. H. Ribeiro, F. Pedregosa, P. van Mulbregt, and SciPy 1.0 Contributors. SciPy 1.0: Fundamental Algorithms for Scientific Computing in Python. *Nature Methods*, 17:261–272, 2020.
- [80] C. R. Harris, K. J. Millman, S. J. van der Walt, R. Gommers, P. Virtanen, D. Cournapeau, E. Wieser, J. Taylor, S. Berg, N. J. Smith, R. Kern, M. Picus, S. Hoyer, M. H. van Kerkwijk, M. B., A. Haldane, J. Fernández del Río, M. Wiebe, P. Peterson, P. Gérard-Marchant, K. Sheppard, T. Reddy, W. Weckesser, H. Abbasi, C. Gohlke, and T. E. Oliphant. Array Programming with NumPy. *Nature*, 585(7825):357–362, September 2020.
- [81] R. d. L. Kronig. On the Theory of Dispersion of X-Rays. *Josa*, 12(6):547–557, 1926.
- [82] E. C. Titchmarsh. *Introduction to the Theory of Fourier Integrals*. Oxford, 1948.